Theses and Dissertations          1. Thesis and Dissertation Collection, all items

2004-06

# Identification of deformation mechanisms during bi-axial straining of superplastic AA5083 material

Fowler, Rebecca M.

Monterey, California. Naval Postgraduate School

http://hdl.handle.net/10945/1204

# NAVAL POSTGRADUATE SCHOOL

## MONTEREY, CALIFORNIA

# THESIS

**IDENTIFICATION OF DEFORMATION MECHANISMS DURING BI-AXIAL STRAINING OF SUPERPLASTIC AA5083 MATERIAL**

by

Rebecca M. Fowler

June 2004

Thesis Advisor:                     Terry McNelley

THIS PAGE INTENTIONALLY LEFT BLANK

| REPORT DOCUMENTATION PAGE | | | *Form Approved OMB No. 0704-0188* |
|---|---|---|---|
| Public reporting burden for this collection of information is estimated to average 1 hour per response, including the time for reviewing instruction, searching existing data sources, gathering and maintaining the data needed, and completing and reviewing the collection of information. Send comments regarding this burden estimate or any other aspect of this collection of information, including suggestions for reducing this burden, to Washington headquarters Services, Directorate for Information Operations and Reports, 1215 Jefferson Davis Highway, Suite 1204, Arlington, VA 22202-4302, and to the Office of Management and Budget, Paperwork Reduction Project (0704-0188) Washington DC 20503. |

**1. AGENCY USE ONLY** *(Leave blank)*

**2. REPORT DATE**
June 2004

**3. REPORT TYPE AND DATES COVERED**
Master's Thesis

**4. TITLE AND SUBTITLE**: Identification of Deformation Mechanisms During Biaxial Straining of Superplastic AA5083 Material

**5. FUNDING NUMBERS**

**6. AUTHOR(S)** Rebecca Fowler

**7. PERFORMING ORGANIZATION NAME(S) AND ADDRESS(ES)**
Naval Postgraduate School
Monterey, CA 93943-5000

**8. PERFORMING ORGANIZATION REPORT NUMBER**

**9. SPONSORING /MONITORING AGENCY NAME(S) AND ADDRESS(ES)**
N/A

**10. SPONSORING/MONITORING AGENCY REPORT NUMBER**

**11. SUPPLEMENTARY NOTES** The views expressed in this thesis are those of the author and do not reflect the official policy or position of the Department of Defense or the U.S. Government.

**12a. DISTRIBUTION / AVAILABILITY STATEMENT**
Approved for public release; distribution is unlimited.

**12b. DISTRIBUTION CODE**

**13. ABSTRACT (maximum 200 words)**

This study evaluated dome test samples of a superplastic AA5083 aluminum alloy deformed at nominally constant strain rates under biaxial strain conditions. Dome test samples resulted from gas-pressure forming of sheet material; for this study, samples were deformed at strain rates corresponding either to grain boundary sliding or dislocation creep control of deformation. Orientation Imaging Microscopy was utilized to determine texture development, grain size and grain-to-grain misorientation angle distributions for locations located along a line of latitude of the dome samples. The goal was to identify the location of the transition from grain boundary sliding to dislocation creep. Grain boundary sliding, which dominates at lower strain rates, can be recognized by a randomized texture and a higher concentration of high disorientation angles. Dislocation creep, which dominates at higher strain rates, is characterized by fiber texture formation and development of a peak at lower angles in the grain-to-grain misorientation angle distribution.

**14. SUBJECT TERMS** Superplasticity, Superplastic deformation, AA 5083, OIM, grain boundary sliding, dislocation creep, biaxial strain

**15. NUMBER OF PAGES** 69

**16. PRICE CODE**

| **17. SECURITY CLASSIFICATION OF REPORT**<br>Unclassified | **18. SECURITY CLASSIFICATION OF THIS PAGE**<br>Unclassified | **19. SECURITY CLASSIFICATION OF ABSTRACT**<br>Unclassified | **20. LIMITATION OF ABSTRACT**<br>UL |
|---|---|---|---|

NSN 7540-01-280-5500

Standard Form 298 (Rev. 2-89)
Prescribed by ANSI Std. 239-18

i

THIS PAGE INTENTIONALLY LEFT BLANK

**IDENTIFICATION OF DEFORMATION MECHANISMS DURING BI-AXIAL STRAINING OF SUPERPLASTIC AA5083 MATERIAL**

Rebecca M. Fowler
Ensign, United States Navy
Undergraduate (B.S.), Worcester Polytechnic Institute, 2003

Submitted in partial fulfillment of the
requirements for the degree of

**MASTER OF SCIENCE IN MECHANICAL ENGINEERING**

from the

**NAVAL POSTGRADUATE SCHOOL
June 2004**

Author:          Rebecca Fowler

Approved by:     Terry McNelley
                 Thesis Advisor

                 Prof. Anthony J. Healey
                 Chairman, Department of Mechanical and
                 Astronautical Engineering

THIS PAGE INTENTIONALLY LEFT BLANK

# ABSTRACT

This study evaluated dome test samples of a superplastic AA5083 aluminum alloy deformed at nominally constant strain rates under biaxial strain conditions. Dome test samples resulted from gas-pressure forming of sheet material; for this study, samples were deformed at strain rates corresponding either to grain boundary sliding or dislocation creep control of deformation. Orientation Imaging Microscopy was utilized to determine texture development, grain size and grain-to-grain misorientation angle distributions for locations located along a line of latitude of the dome samples. The goal was to identify the location of the transition from grain boundary sliding to dislocation creep. Grain boundary sliding, which dominates at lower strain rates, can be recognized by a randomized texture and a higher concentration of high disorientation angles. Dislocation creep, which dominates at higher strain rates, is characterized by fiber texture formation and development of a peak at lower angles in the grain-to-grain misorientation angle distribution.

THIS PAGE INTENTIONALLY LEFT BLANK

# TABLE OF CONTENTS

THIS PAGE INTENTIONALLY LEFT BLANK

# LIST OF FIGURES

THIS PAGE INTENTIONALLY LEFT BLANK

# LIST OF TABLES

THIS PAGE INTENTIONALLY LEFT BLANK

# ACKNOWLEDGMENTS

As the author of this paper I would like to acknowledge first and foremost my advisor, Professor Terry McNelley, for making this research possible and for teaching me both in and out of the classroom.

Secondly I would like to extend my deepest thanks to Dr. Keiichiro Oishi, for his infinite amounts of patience and microscopy knowledge.

Finally I would like to thank all those who made this possible and who kept me going through the many long hours, especially Matt Shea for being my rock, Kristen Deffenbaugh for her amazing mind and endless patience, and the rest of the E-Funk crew for keeping me mostly sane.

THIS PAGE INTENTIONALLY LEFT BLANK

# I.  INTRODUCTION

There is a push in today's automotive industry to replace steels with suitable, lighter metallic materials.  With today's increasing fuel costs, lighter cars would require less energy to move, thereby saving direct consumer costs as well as natural resources.  Aluminum is one such metal under consideration because of its potential formability and lightness.  Incorporating aluminum into automotive bodies requires that increased costs for this not be so great that vehicle prices become prohibitive or such that no net savings can be realized.

An important concern in choosing a suitable aluminum alloy is corrosion resistance.  Aluminum-magnesium alloys such as AA5083 are well suited in this area due to their general resistance to corrosion, coupled with their moderate strength and weldability [Ref. 1, 2].  However, this material has insufficient formability and, as Harrell states [Ref. 3],

> Aluminum alloys have not been used more widely for many structural and transportation applications because alloys of sufficient strength may be difficult to form using conventional die forming methods, and alloys that are easily formed often do not possess sufficient strength.

Traditional forming practices present inherent difficulties when used with aluminum.  Extrusion and rolling can only produce limited shapes.  Milling produces excessive waste and casting often results in porosity problems and low strength.  Consequently, new methods such as superplastic forming, electromagnetic forming, and hydroforming are gaining increasing attention [Ref. 4].  Aluminum alloys are currently used in aerospace applications because the weight advantages are more important than the added costs associated with utilization of this metal.  Thus, advances in forming techniques would have a significant technological impact on both automotive and aerospace production.

Superplastic forming (SPF) requires large tensile elongations because material will be deformed by subjecting a heated sheet of superplastic aluminum to a pressure differential in order to form complex shapes.  The related process

for forming steel parts utilizes stamping with mated dies. SPF requires only one die per part and the die not be as hard as those used for steels. An illustration of SPF is depicted below in Figure 1.
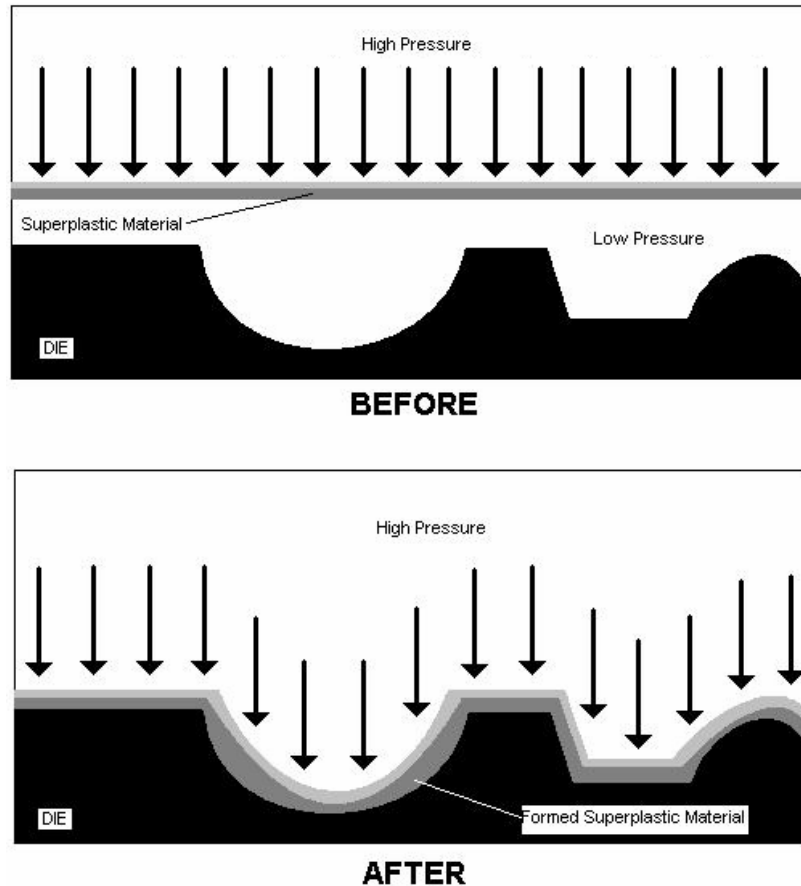


Figure 1: Schematic of Superplastic Forming Process ([From Ref. 5])

During SPF, the sheet initially deforms under biaxial strain conditions. After it comes into contact with the die forming conditions become more complex. The significant concerns generated by SPF are being addressed in ongoing research, such as sheet thinning and cavitation. Throughout forming, the sheet thins in a non-uniform manner which leads to areas of reduced strength that are more prone to failure. In addition to thinning, the onset of cavitation within the material also decreases the strength and is most prominent at the thinnest sections.

Finally, in order to achieve the desired forming characteristics, SPF has been carried out at generally low strain rates, which dictate long forming times. This has been a deterrent to wide-spread industrial implementation. If higher forming rates could be employed, lower forming times would result [Ref 6]. The requirement for generally low forming rates reflects that two independent mechanisms contribute to the overall rate of deformation. These are grain boundary sliding (GBS) at low rates and dislocation creep at high rates. Since grain boundary sliding generally gives the highest elongations it is necessary to deform at rates within the GBS regime [Ref. 7].

This report considers the effects of strain rate over a wide range during biaxial forming in an effort to understand the effect of strain rate on superplastic forming under such conditions. Previous studies have analyzed superplastic deformation under unixial tension and identified methods to differentiate between the GBS and dislocation mechanisms. The aim of this research was to assess whether these methods could be employed on a sample formed under biaxial strain conditions and to identify in each sample where the possible transition between deformation mechanisms occurred.

THIS PAGE INTENTIONALLY LEFT BLANK

## II.    BACKGROUND

### A.    SUPERPLASTICITY

"Superplasticity is the ability of a polycrystalline material to exhibit, in a generally isotropic manner, very high tensile elongations prior to failure [Ref. 7]." Typically elongations of 10% to 100% are observed in engineering metals, while elongations >200% generally classify a material as superplastic.   It is not uncommon to observe tensile elongations greater than 1000%, and the maximum superplastic elongation recorded is 8000% in a commercial bronze sample.    There are two types of superplastic behavior: fine-structure superplasticity (FSS), which will be the focus of this research, and internal-stress superplasticity (ISS).   As suggested by the name, a refined grain structure is imperative for FSS.   Normally, FSS metals exhibit equiaxed grains less than 10 um in diameter and less than 1 um in ceramics [Ref 7].   .

For tensile deformation the dependence of the flow stress, σ, on the true strain rate, έ, is described by the equation:

$$\sigma = K\dot{\varepsilon}^{m}$$                    Equation II-1

where K is a material constant and *m* is the strain-rate sensitivity coefficient. Most metals and their alloys exhibit *m* values of less than 0.2.   In general, superplastic materials evidence sensitivity coefficients of greater than 0.33. However, although m values in this range are necessary for superplasticity, they do not guarantee its occurrence [Ref. 7, 8].

During elevated temperature deformation of a superplastic material the two active deformation mechanisms are GBS (accommodated by slip), and dislocation creep.  These mechanisms operate independently and therefore have additive effects [Refs. 2, 7, 8, 9, 10].  A number of models have been suggested to describe the additive effects of GBS and dislocation creep.   The general assumption of each model is that both creep mechanisms behave according to

Equation II-1 but having the corresponding values of K and *m*.  A more comprehensive model incorporating temperature dependence has the form [Ref. 7]:

$$\frac{\dot{\varepsilon}}{D_L} = \frac{10^{11}}{b^2}\left(\frac{\sigma}{E}\right)^{1/m_\perp} + \frac{2\cdot 10^9}{L^2}\left(\frac{\sigma}{E}\right)^{1/m_{gbs}}$$

Equation II-2

Where $D_L$ is the lattice diffusivity, b is the Burger's vector, E is the Young's modulus, and L is the mean linear intercept grain size.  Dislocation creep and grain boundary sliding are then expressed in the right hand side of the equation as the first and second terms, respectively.  However, use of this model requires that the rate-controlling step be known [Refs. 2, 7, 8, 9, 10].

Application of equation II-2 for isothermal conditions is depicted in Figure 2.  There are three regions depicted in this plot.  Region one is characterized by high *m* values, superplastic ductility, and the dominance of GBS.  Grain boundary sliding usually occurs with a strain-rate sensitivity coefficient of about 0.5 and, as shown, is dominant at low deformation rates.  The equiaxed grain structure in FSS along with the prevalence of high-energy boundaries accommodates sliding under the proper shearing conditions.
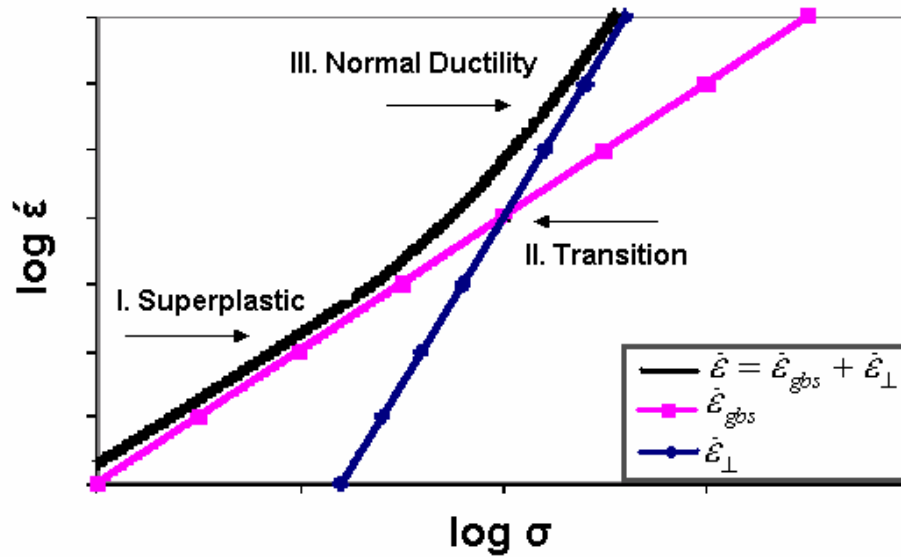


Figure 2    Schematic plot depicting three deformation regions experienced in superplastic forming ([After Ref. 3])

6

As the strain rate increases a transitional stage is observed. The strain rate at the transition from superplasticity to normal tensile elongation is inversely proportional to the grain size.   Through the transition region, grain boundary sliding gives way to dislocation creep as the dominant deformation mechanism. The strain rate sensitivity then becomes approximately 0.2 and the material shifts from superplastic flow to normal ductility [Refs. 7, 11].


## B.    MICROSCOPY METHODS

Research in this area was completed primarily through the use of analytical electron microscopy.   Scanning electron, backscatter electron, and orientation imaging microscopy were all implemented over the course of this study.

### 1.    Scanning Electron Microscope (SEM)

Scanning Electron Microscopy employs an electron beam and various signals to create images of sample surfaces.  As shown in Figure 3, an electron gun generates a beam which is focused through a series of lenses and magnetic coils.   The beam interacts both elastically and inelastically with electrons and atoms in the specimen, and causes specimen electrons and x-rays to be emitted [Ref. 12].   The inelastic collisions generate secondary electrons that typically have energy less than 50 eV.  An electron detector subsequently converts the secondary electrons to an electrical signal which is, in turn, fed to a signal processing unit to generate the corresponding image [Ref. 13].
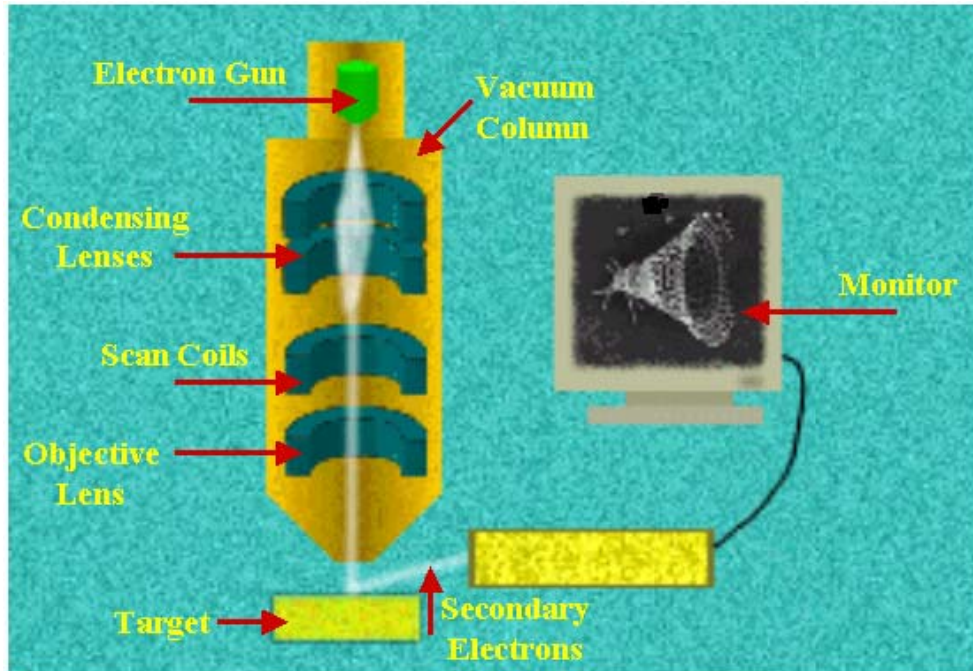
Figure 3        SEM schematic ([After Ref. 13])

While X-rays can be used to verify the composition of a material, they were not useful in the progress of this study.  Secondary electron images and backscatter images which provide topographical information, however, were used to verify Orientation Imaging techniques and identify second phase particles and cavities.

### 2.        Orientation Imaging Microscopy and Analysis

Orientation Imaging Microscopy, or OIM, uses the SEM as a point probe of the local lattice orientation.  It is carried out by displacing the electron beam from point to point in a raster pattern as depicted below.
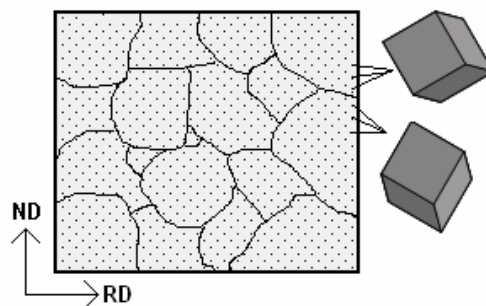


Figure 4        Schematic of OIM raster pattern

8

Orientation measurements are then made at each point through electron backscatter diffraction patterns (EBSP) which will be discussed further in the experimental section of this paper. The measurements taken from a given scan area are then compiled into a data file which can be analyzed by the software. This software allows for a grain-specific microstructure representation where a grain is considered an area of constant lattice orientation. Once the orientations of two points are known, the misorientation angle between them can be calculated [Ref. 15, 16, 17, 18].

OIM software evaluates EBSPs by locating the Kikuchi bands, measuring the angle between the bands, and then comparing them to a set of reference patterns. The computer locates the bands through the application of the Hough transform which translates the bands into points in Hough space. These are more readily identified and catalogued by the software. The angles are then calculated and the comparison between experimental and theoretical patterns is carried out. This allows for determination of microstructural phase and crystallographic orientation [Ref. 15, 16, 17, 18]. An example of a grain map generated by OIM software is shown in Figure 5.
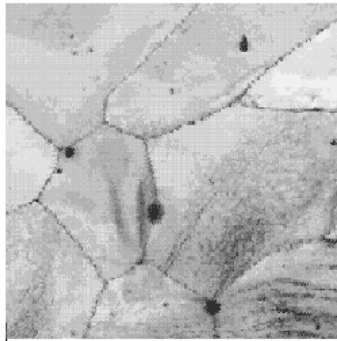


Figure 5    Example of a grain map created with OIM software ([From Ref. 16])

In general, several crystallographically equivalent rotations will bring two crystals in coincidence. Each rotation may be described by a misorientation angle and corresponding rotation axis. For the purpose of this study, however, the misorientation angle will be defined as the smallest among these angles. The user defines a grain tolerance angle which stipulates the maximum

misorientation necessary to identify two lattice structures as separate grains. Thus, grain boundaries divide two areas of differing lattice orientations. Due to crystal symmetry, misorientation angles for a cubic material range from 0 to 62.8° and a compilation of all the misorientation data available for a scan area is represented in a histogram as shown below. The histogram shows the relative number of boundaries as a function of misorientation angle. The diagram below indicates a predominance of low-angle boundaries [Ref. 15, 16, 17, 18].
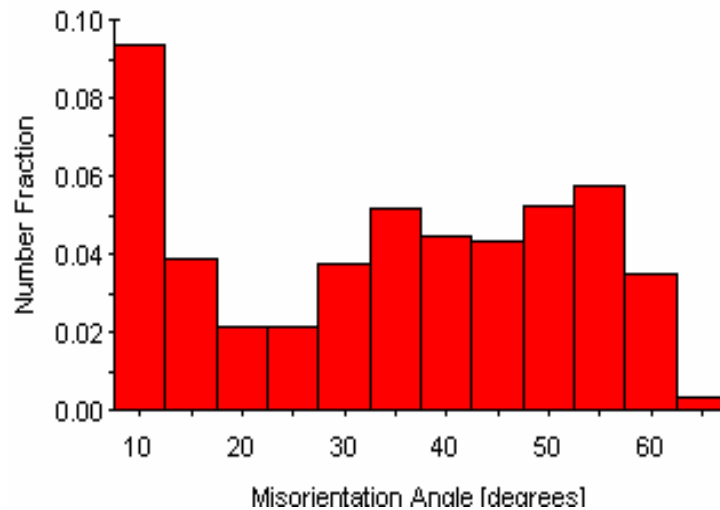


Figure 6        Example of a histogram generated by OIM software ([From Ref. 16])


"Texture analysis is a statistical methodology for analyzing the distribution of crystallographic orientation in polycrystalline materials [Ref. 16]." Texture plots are stereographic projections of specified planes. The stereographic projections are coupled to a set of reference axes and thus describe the spatial distribution of lattice orientation. The following figure shows an example of both a random texture, generated during this research, and a fibered, or axisymmetric, texture as depicted in the OIM Analysis Manual [Ref. 16]. The color plots allow the user to see the relative intensity of points at a given location.

10
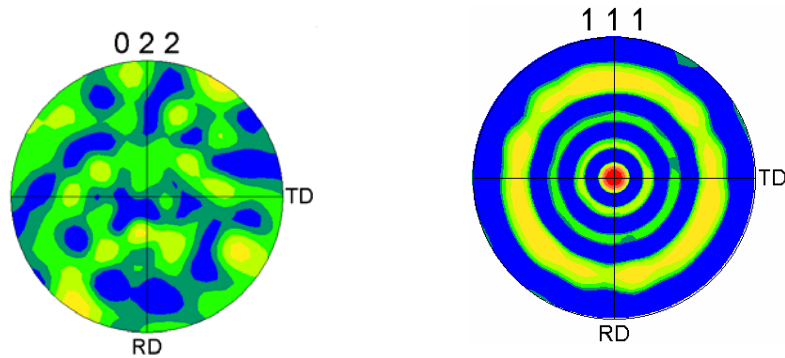
Figure 7    Example of (a) a random texture and (b) a fiber texture ([From Ref. 16]).

Texture can also be represented in a polar plot as shown in Figure 8.  The chart shows the intensity as a function of location by taking the integration of a pole figure about the azimuthal on the stereographic projection.  The use of these charts allows the apparent texture from different planes to be plotted on the same graph [Ref. 16].
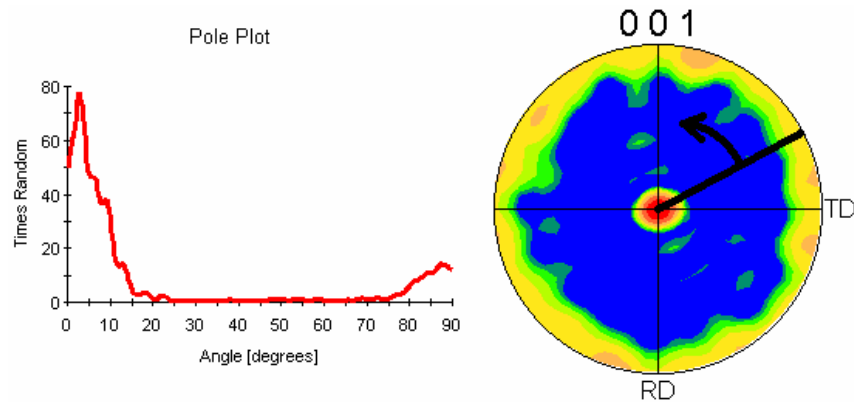


Figure 8    Example of a polar plot and the corresponding texture ([From Ref. 16]).

## C.    PREVIOUS STUDIES

Previous studies in this area have looked at the effects of superplasticity as it pertains to cavity growth, forming conditions, dynamic recrystallization, and deformation mechanisms.

### 1. Cavitation

Studies by Verma *et al.* [Ref. 8] on AA 5083 have shown that cavitation increases with increasing strain and strain rate as depicted in Figure 9, which illustrates the general trend of their results.  The effect of strain and strain rate on cavitation in other materials has also shown similar results [Refs. 8, 20].  Studies done on materials in both uniaxial and equibiaxial tension have shown that under optimum conditions, the amount of cavitation only slightly increases from uniaxial testing to equibiaxial testing [Ref. 6].
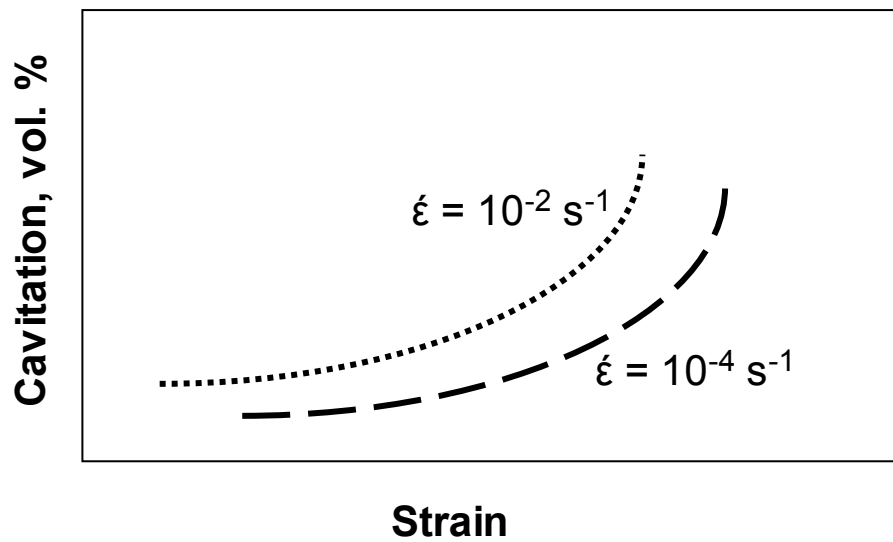


Figure 9        Schematic representation of strain and strain rate effects on cavitation ([After Ref. 8]).

### 2. Grain Growth

It has also been shown that during superplastic forming, a continuous dynamic recrystallization process occurs [Refs. 8, 19].  The investigation on AA5083 noted above and conducted by Verma *et al.*, 1996, examines the occurrence of both static and dynamic grain growth as functions of strain rate and time.  They observed that dynamic grain growth was significantly greater than static grain growth.  The researchers also found that higher strain rates showed an increased growth rate during dynamic grain growth as represented in Figure 10 [Ref. 8].

12
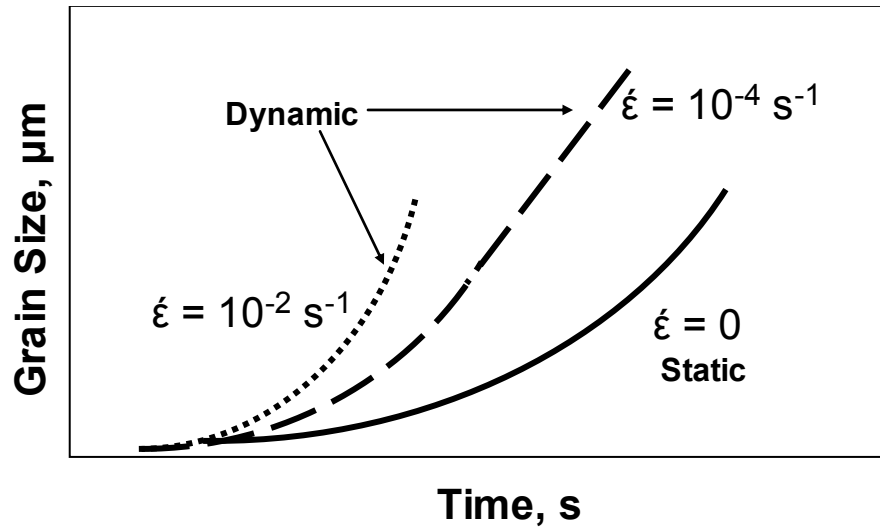
Figure 10    Schematic representation of time and strain rate effects on grain growth ([After Ref. 8]).

### 3.    Texture

Past research on texture development has resulted in the following three findings.  First, thermomechanical processing techniques such as hot rolling can cause a weak apparent orientation in sheet materials [Refs. 16, 21, 22].  This results in a faint texture during orientation imaging work.  Second, grain boundary sliding causes a rotation of the grains themselves which generates an indiscriminate orientation structure and consequently a random texture [Refs. 11, 17, 21, 23, 24].  Finally, dislocation creep causes distortions within the lattice and a preferred orientation of grains which produces a fiber texture during OIM [Refs. 11, 17].

Previous studies conducted at this university on AA5083 in uniaxial tension have confirmed these findings.  The most recent reports were conducted using the same SEM and OIM software used in this research.  These studies verified the independent and additive effects of grain boundary sliding and dislocation creep through texture measurements.  It was noted that the grain rotation experienced during GBS generates a randomized texture in the material while maintaining an equiaxed grain shape.  Dislocation creep, on the other hand, causes lattice rotations within the grain which lead to grain distortion and

13

result in a preferred orientation, namely a <111> fiber orientation and a {100}<100> cube component, as shown in the figure below [Refs. 3, 7, 17]. This combination was shown to allow compatible deformation under uniaxial tensile straining conditions [Ref. 10]. Harrell, 2001, observed that dislocation creep exhibits the characteristic formation of elongated grains with fine subgrains distinguished by misorientation angles less than 15˚. He also noted that cold-rolled materials exhibit a banded structure prior to deformation [Ref. 3].
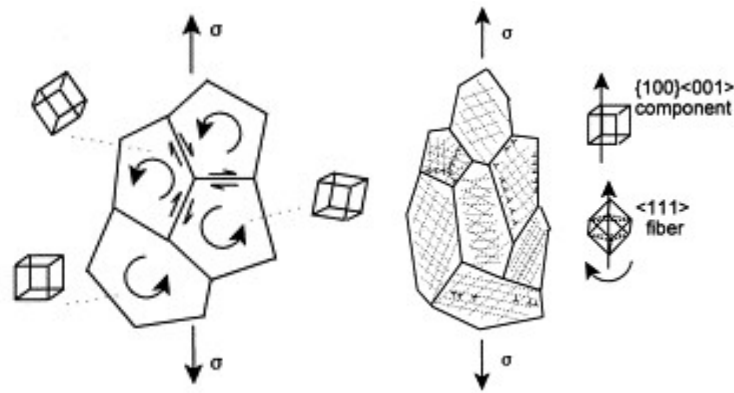


Figure 11    Schematics of the microstructural effect of (a) Grain Boundary Sliding and (b) Dislocation Creep ([From Ref. 17]).

# III.    EXPERIMENTAL PROCEDURE

## A.    OVERVIEW

This thesis included work done on two AA 5083 dome samples, provided by the University of Texas, Austin.  The samples, designated 978931-5 and 978931-I, were formed at strain rates of $3\times10^{-4}$ s$^{-1}$ and $10^{-2}$ s$^{-1}$ respectively.  Both samples were produced under biaxial strain conditions.  One objective of this research was to confirm that the sample formed at the slower strain rate underwent deformation in the grain boundary sliding regime only.  The second goal was to determine if it is possible to identify the location where dislocation deformation replaced grain boundary sliding as the dominant deformation mechanism.

## B.    SAMPLE SET

A pneumatic bulge test was employed to form the samples, during which a preheated AA5083 blank was clamped between a lower platen and an upper cylindrical forming die, then subjected to a constant gas pressure as depicted in Figure 12.  The die holding the sample is contained in a furnace able to maintain uniform temperatures.
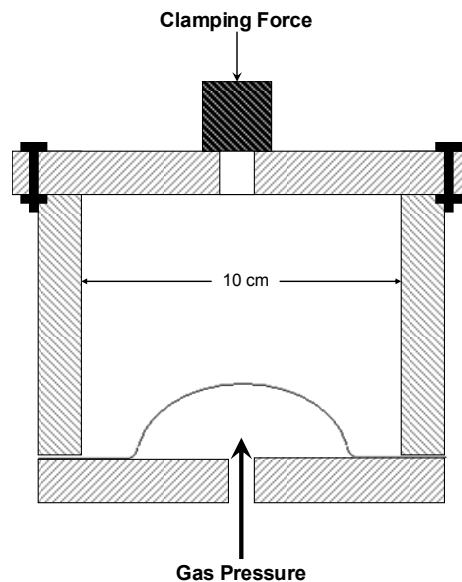
Figure 12     Schematic of bulge forming process ([After Ref. 26])

"The height of the resulting dome-shaped sample is taken as a relative measure of the material's formability… The bulge test also allows a region of the sample to be tested in biaxial stretching, which is more representative of the initial stages of SPF deformation conditions than uniaxial tension [Ref. 26]." Strain rates in bulge samples vary up the dome from 0 to some maximum value. Bulge samples are then classified by a nominal strain rate that occurs in the mid-latitudes of the deformed sample. Although a sample strain rate may indicate that it underwent deformation only in the GBS regime, it is possible that the higher strain rate values experienced above the mid-latitudes were in the dislocation creep dominated regime. A schematic representation of this is shown in Figure 13.
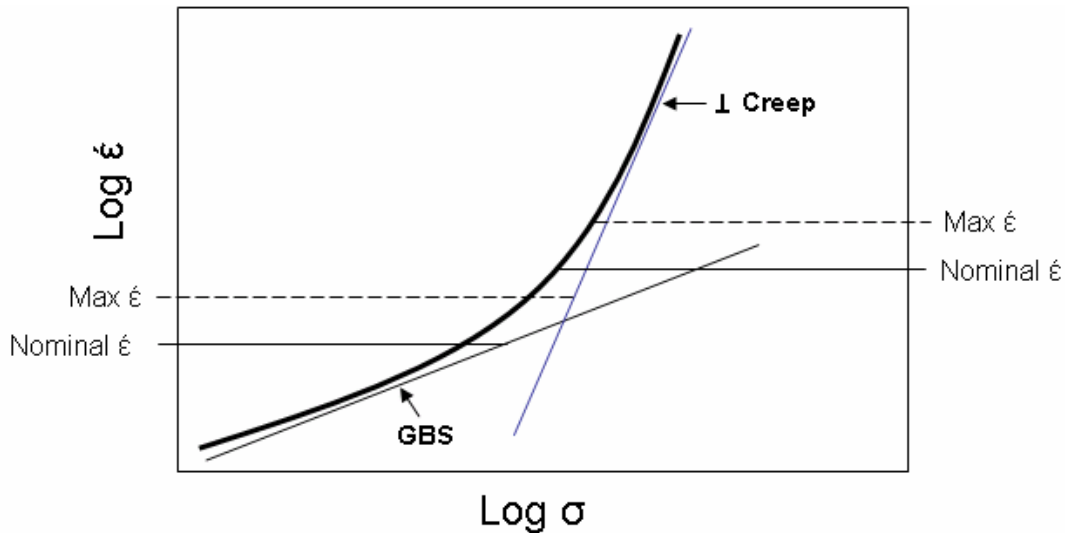


Figure 13     Schematic representation of nominal strains

The tool diameter was 10 cm and the initial sheet thickness was 0.125 cm. Figure 14 shows bulge tests at various times in the forming process.



Figure 14     Bulge samples at various times during the forming process.

Both of the sample domes had already been sectioned in two halves approximately through the pole when received. Prior to forming, a uniform grid of circles 0.254 cm in diameter had been etched on the surface of the aluminum sheet material. This allowed for the measurements of local strains as well as verification of rolling direction and transverse direction in the deformed dome samples. A band saw was used to cut a strip approximately 1/2 inch across, as shown in Figure 15 below.
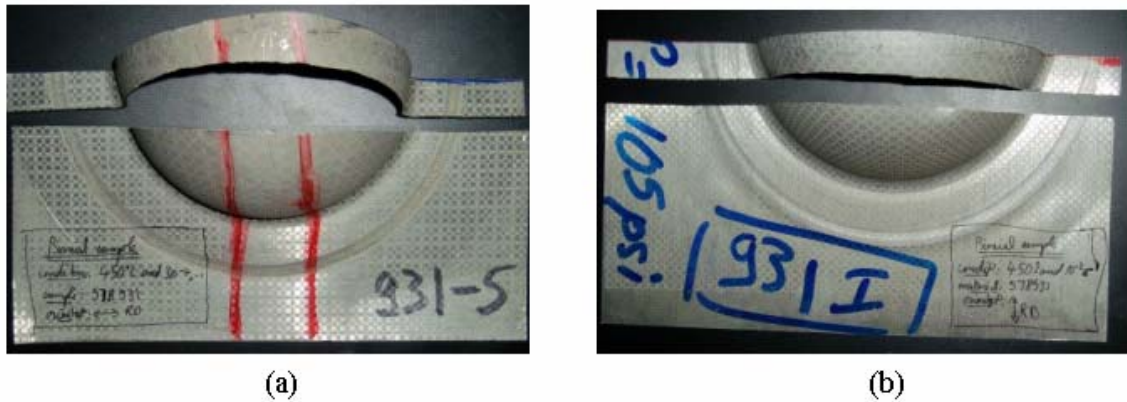


Figure 15    AA 5083 Dome Samples (a) $3x10^{-4}$ strain rate, (b) $10^{-2}$ strain rate

The etched circles were then numbered accordingly as shown in Figure 16 and located at the positions indicated in Table 1. It is important to note that the lower strain rate sample achieved a greater dome height of 5.86 cm, as denoted by position 15 measurement, while the higher strain rate sample achieved a height of 4.93 cm at the same position.
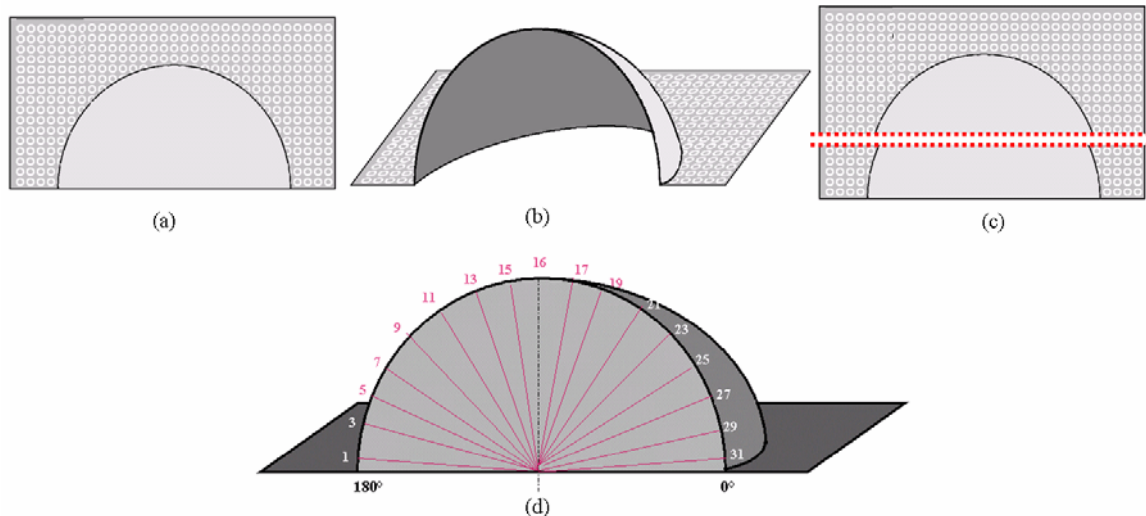
Figure 16    Sample diagram.  (a) Top view, (b) Side view, (c) Initial strip cut, and (d) circle number and locations across dome.

| Position | Radius (cm) | Theta (°) | Position | Radius (cm) | Theta (°) |
|---|---|---|---|---|---|
| 32 | 5.00 | 180 | 32 | 5.00 | 180 |
| 31 | 4.90 | 176 | 31 | 5.06 | 175 |
| 29 | 4.78 | 164 | 29 | 5.07 | 164 |
| 27 | 4.69 | 154.5 | 27 | 5.12 | 153 |
| 25 | 4.68 | 144 | 25 | 5.14 | 143 |
| 23 | 4.67 | 133.5 | 23 | 5.25 | 132 |
| 21 | 4.80 | 121 | 21 | 5.40 | 122 |
| 19 | 4.86 | 108.5 | 19 | 5.56 | 110 |
| 17 | 4.92 | 95.5 | 17 | 5.62 | 97 |
| 16 | 4.89 | 89 | 16 | 5.74 | 92 |
| 15 | 4.93 | 81 | 15 | 5.86 | 84 |
| 13 | 4.82 | 67.5 | 13 | 5.71 | 72 |
| 11 | 4.74 | 55 | 11 | 5.50 | 60 |
| 9 | 4.72 | 44 | 9 | 5.34 | 47 |
| 7 | 4.71 | 34 | 7 | 5.20 | 37 |
| 5 | 4.73 | 23 | 5 | 5.10 | 26 |
| 3 | 4.83 | 13 | 3 | 5.05 | 16 |
| 1 | 4.90 | 3 | 1 | 5.00 | 5 |
| 0 | 5.00 | 0 | 0 | 5.00 | 0 |

Table 1    Position locations by radius and angle of (a) $10^{-2}$ s$^{-1}$ strain rate and (b) $3 \times 10^{-4}$ s$^{-1}$ strain rate.

After recording the angle and radius to each grid circle, a Buehler low-speed saw equipped with a diamond-wafering blade was used to section the samples so that the middle of each segment would correspond to the following

positions: 1; 5; 9; 13; 17; as well as a section from the undeformed region. These locations were chosen to get a representative picture of the evolution of texture and its correspondence to deformation mechanism along the dome. When cutting, care was taken to keep the blade at least 0.5 cm away from the desired location, thus avoiding damage to the microstructure due to sectioning. After the 6 samples were cut, they were again cut parallel to the sample surface at a distance of approximately 0.5 cm. This was once more done to avoid damage to the microstructure and to fit sample holder requirements for the OIM.

## C.    SAMPLE PREPARATION

Once the samples had been sectioned, preparation for microscopy work began. During Orientation Imaging Microscopy, electron backscatter diffraction takes place at a depth of only 50 nm below the surface [Ref. 3]. As a result, it is very important that the sample be polished to achieve a uniform flat surface free of residual stress. This is accomplished through grinding and polishing. The grinding began with 500 grit silicon carbide paper and continued with successively finer grits as laid out in Table 2 below. The silicon carbide papers were placed on a Buehler Wheel, set to a speed of 40 rpm, and lubricated with water. It was necessary to avoid the use of excessive downward pressure during grinding to prevent the embedding of abrasives and superficial deformation of the sample surface. After each grinding step, the samples were rinsed with methanol. Following the final grinding step the samples were placed in a beaker of methanol and ultrasonically cleaned for 10 minutes.

| Grit | Wheel Speed | Time |
|------|-------------|------|
| 500 | 40 rpm | 30 sec |
| 1000 | 40 rpm | 30 sec |
| 2400 | 40 rpm | 30 sec |
| 4000 | 40 rpm | 30 sec |

Table 2        Grinding Procedure

Polishing is necessary remove all remaining distortions after grinding. The samples were first polished with a 1 μm colloidal silica suspension on a polishing cloth. The cloth was placed on a Buehler Wheel and set to 50 rpm. Samples were polished until all evidence of grinding was removed. A Buehler Electromet 4 Electropolisher was employed to accomplish this task. Using a 20% Perchloric Acid – 70% Ethanol – 10% Glycerol electrolyte solution that was cooled to –25° C, the samples were polished for two 10 second intervals. The samples were then quickly placed in a beaker filled with methanol to prevent surface oxidation prior to examination by Orientation Imaging Microscopy as described in the background section.

## D.     ELECTRON BACKSCATTER DIFFRACTION

Electron backscatter diffraction (EBSD) is accomplished by subjecting a sample to a focused electron beam. The electrons then interact with the material and are diffracted to create a pattern consistent with the local crystallographic orientation. The patterns are comprised of several intersecting lines which are known as Kikuchi bands. The pattern can be indexed by analyzing the arrangement of the Kikuchi bands [Ref. 15]. EBSD was carried out using a TOPCON SM-510 Scanning Electron Microscope (SEM). The SEM is equipped with a tungsten filament and was operated at an accelerating potential of 20 kV.

After the samples were polished and placed in the methanol they were brought to the SEM lab. The samples were then dried and mounted in the SEM using a sample holder that maintains the examination surface at a 70° angle to the incident electron beam. This allows Bragg Diffraction to be carried out without having to rock the electron source. The SEM was then brought up to the desired accelerating potential and the Tungsten filament brought up to saturation. The spot size was generally set to either 10 or 11, 10 being the preferred spot size since it produced the lowest signal to noise ratio. After locating the desired position on the sample, the sample was brought into focus.

## E.    ORIENTATION IMAGING MICROSCOPY

Orientation Imaging Microscopy (OIM) software was employed to capture and analyze the EBSD patterns, known as EBSPs.  A phosphor screen is positioned near the sample to catch the image of the diffracted electrons (Figure 17).  A low-light camera is then utilized to acquire the image on the phosphor screen for indexing by the OIM software.  Eight frames are received and then averaged by the computer and the resulting Kikuchi band is indexed for that point.  Using the OIM software, sample scans were set to cover a 250 µm by 75 µm region, with a step size of 1 µm.  The long leg of the scan ran parallel to the transverse direction in the higher-strain-rate samples and parallel to the rolling direction in the lower-strain-rate samples.  After the scan was completed, data analysis began.
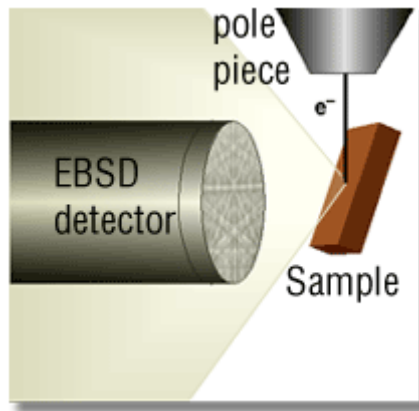


Figure 17     Electron backscatter diffraction schematic ([From Ref. 12]).

The data was cleaned up to eliminate noise and improve contrast.  The grain tolerance was set to 2 with a minimum grain size of 1, as well as criteria stipulating that a minimum confidence index (CI) of 0.1 be met.  The data was then rotated to coincide with axis used by the OIM.  In the higher strain rate sample this required 2 rotations of approximately 90 about both the normal direction (ND) and the rolling direction (RD).  In the lower strain rate sample this required only one rotation of approximately 90 about the normal direction (ND).

THIS PAGE INTENTIONALLY LEFT BLANK

# IV.   RESULTS

## A.   GRAIN SHAPE AND SIZE

As discussed in the background section, grain boundary sliding under uniaxial tension is characterized by equiaxed, slightly elongated grains and grain growth during deformation.  In contrast, dislocation creep results in an elongated grain structure that contains subgrains of misorientation angle less than 15°.  Grain growth typically is less evident during dislocation creep deformation than during GBS.  In an effort to determine the dominant deformation mechanism across the dome, grain size and shape measurements were made using the OIM software for materials deformed under nominally GBS and dislocation creep conditions.  A representative overview of these analyses is shown in and Figure 18 and Figure 19.
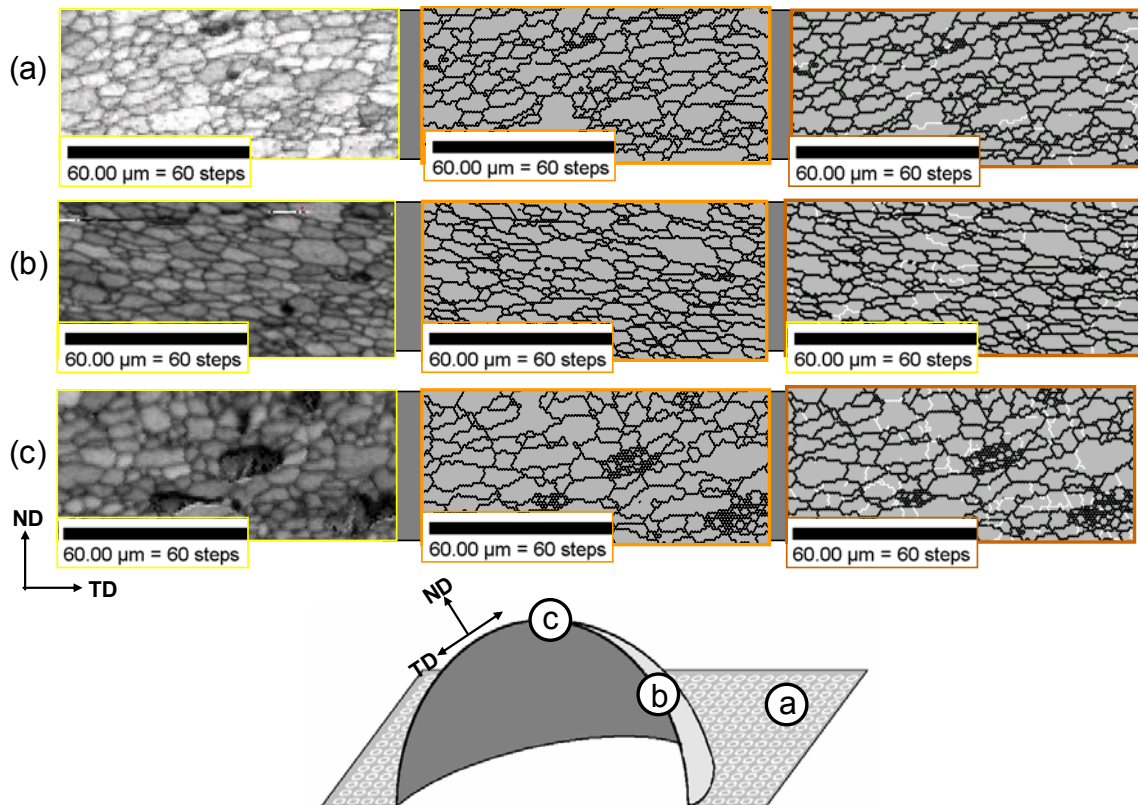


Figure 18     Grain Size and Shape Data for sample deformed at $3 \times 10^{-4}$ s$^{-1}$

The data in Figure 18 were taken from the sample of nominal strain rate $3\times10^{-4}$ s$^{-1}$, which showed visible signs of failure in the pole region prior to sectioning. The final dome height was about 5.8 cm. Row (a) in this figure corresponds with data collected in the undeformed region of the sample, while row (b) relates to data gathered at the mid-latitude of the sample and row (c) is data from the pole region. The first column of this figure contains Image Quality (IQ) maps generated with OIM software for each region. In the second column only grain boundaries greater than 15° are included, thereby rendering the overall grain shape. The final column also includes boundaries ≤15° and thus shows the formation of subgrains within the grain structure. The red lines indicate grain boundaries less than 15°, thus the occurrence of subgrains. The development of cavitation is apparent in all three columns of data. The diagram shows that the normal direction is perpendicular to the local sheet normal while the rolling direction runs parallel.

The images in row (a) represent material that has experienced mainly annealing alone and show a refined, recrystallized grain structure. The grains are somewhat elongated in the prior rolling direction and there are a few low-angle boundaries present. The darkest regions in the IQ map are likely particles or small cavities. At the mid-latitude region (row b), some grain growth is evident, as well as grain elongation. Grain growth is most apparent in the grain maps showing boundaries >15° (middle column). When all boundaries are considered (right-hand column) it appears that subgrain boundaries are forming even though deformation conditions correspond to GBS. Further grain growth is apparent to the right-hand side of all images in row (c), and subgrain formation is also evident in regions between cavities. Thus, local conditions may vary significantly from the nominal conditions for this material.
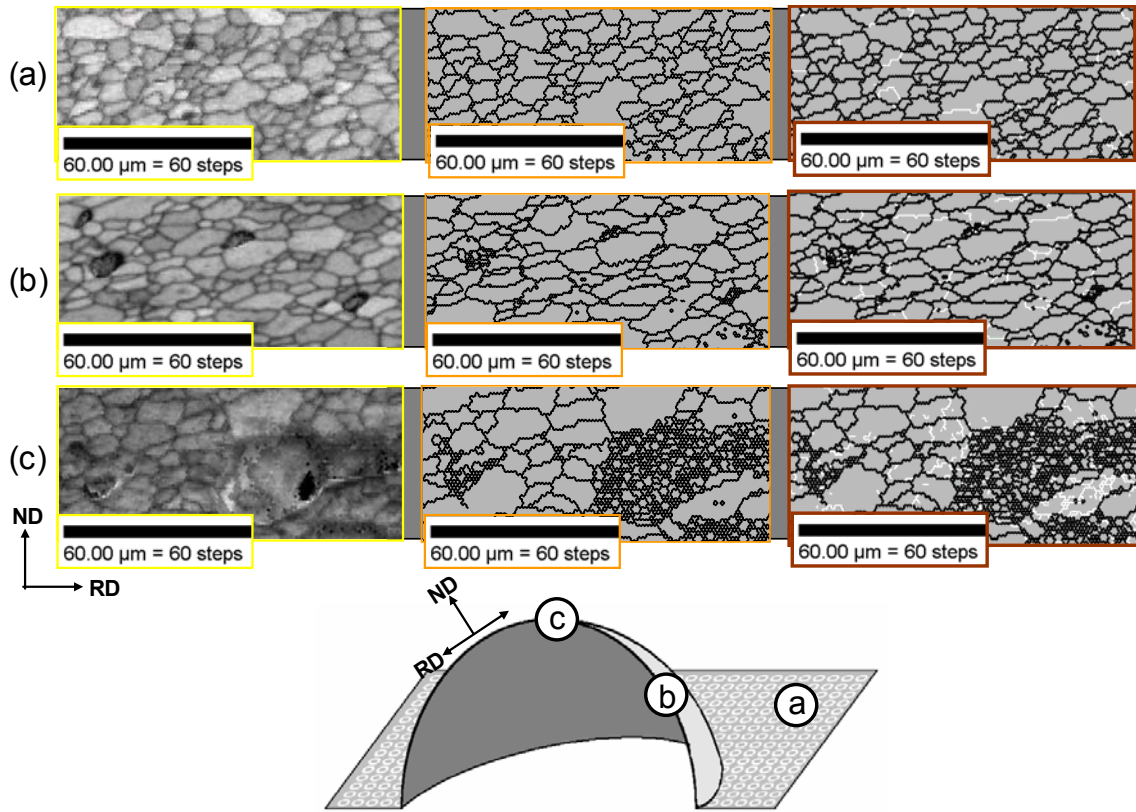
Figure 19     $10^{-2}$ Grain Size and Shape Data

The data in Figure 19 were taken from the sample formed at the higher nominal $\dot{\varepsilon}$, $10^{-2}$ s$^{-1}$. Unlike the previous sample, this one did not show any outward signs of failure prior to sectioning, but the final dome height had reached approximately 4.9 cm, nearly 1 cm less than the previous sample. Row (a) in this figure also corresponds to data collected in the undeformed region of the sample, while row (b) relates to data gathered at the mid-latitude of the sample and row (c) is, again, data from the pole region. The first column of this figure contains Image Quality maps generated with OIM software for each region. The second column is a representation of grain boundaries greater than 15°, depicting overall grain shape. The final column shows the formation of subgrains within the grain structure. The red lines indicate grain boundaries less than 15°, thus the occurrence of subgrains. The development of cavitation is apparent in all three columns of data. As indicated by the inset axes, the normal direction is parallel to the outward sheet normal while the transverse direction runs perpendicular.

25

As indicated in the second column, a fine, relatively equiaxed grain structure is present in the undeformed region; some grain elongation in the prior rolling direction may be observed. Around the mid-latitude region, more grain elongation can be seen along with minor grain growth. At the pole, there is still more grain growth in both the thickness and transverse direction and subgrain boundaries aligned with both directions.

## B.    MISORIENTATION ANGLE

Grain boundary sliding is also characterized by a near random distribution of grain-to-grain misorientations. Conversely, dislocation creep can be distinguished by the appearance of low-angle (0-15˚) boundaries. The charts below represent misorientation calculations taken from the sample deformed at the lower rate.
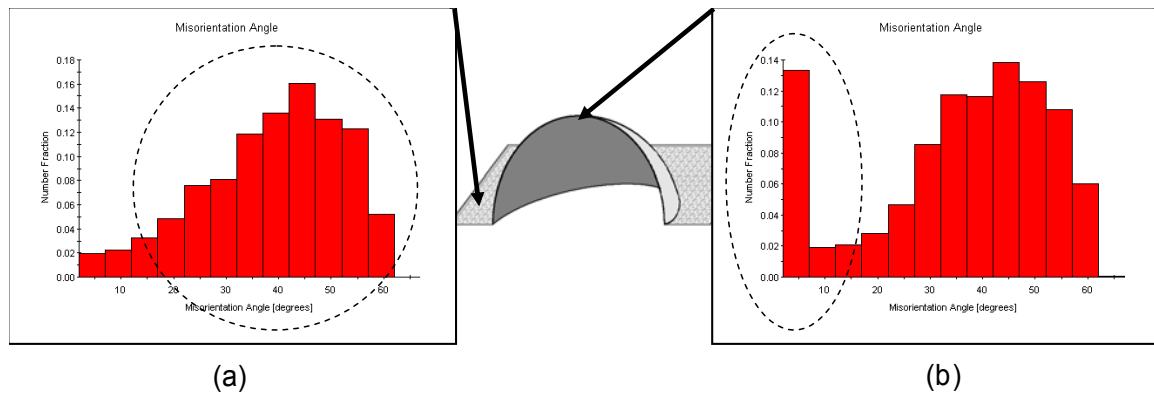


(a)                                                      (b)

Figure 20     Histograms for 3x10-4 s-1 sample depicting (a) high-angle boundaries and (b) the occurrence of low-angle boundaries.

Figure 20(a) shows a random distribution of misorientations in the undeformed region of the sample. Similar calculations up the dome of the sample show the dominance of high-angle boundaries until the pole is reached. Figure 20(b) shows the appearance of low-angle boundaries in the distribution that occurred at the pole of the dome.

Misorientation calculations up the dome are superimposed in Figure 21 and show the distinct change at the pole from grain boundary sliding to

dislocation creep regime. The corresponding histograms for these data are included in Appendix A.
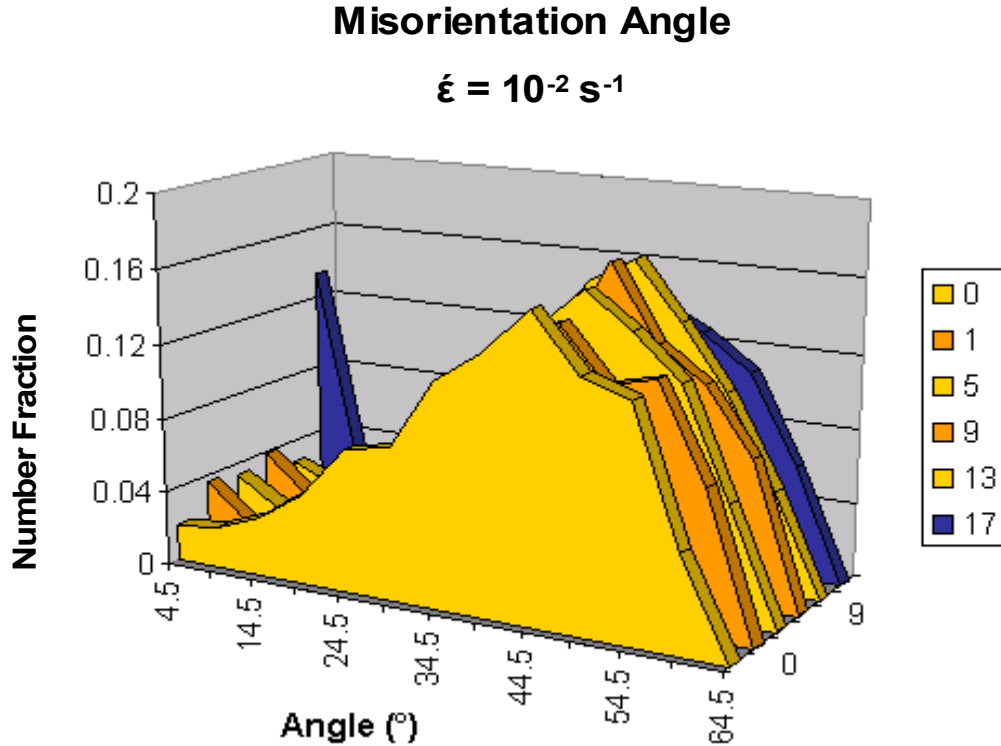
## Misorientation Angle

$\dot{\varepsilon} = 10^{-2}\ s^{-1}$



Figure 21    Misorientation angle distributions for $3 \times 10^{-4}\ s^{-1}$

In this figure, the data denoted '0' are for the undeformed region, and the increasing numbers correspond to the positions laid out in the experimental section; the location denoted '17' is near the pole of the dome. The light colored plots depict a dominance of high-angle boundaries while the dark plot represents the data from the pole area and the development of low-angle boundaries.

The sample deformed at the higher strain rate showed a similar plot for the undeformed region but development of low-angle boundaries at lower latitudes. Figure 22 shows that high-angle boundaries (a) dominate only in the undeformed region and that low-angle boundaries (b) appear around 40-45° up the dome. Misorientation calculations up the dome are shown collectively in Figure 23 and suggest that a transition from GBS to dislocation creep occurred

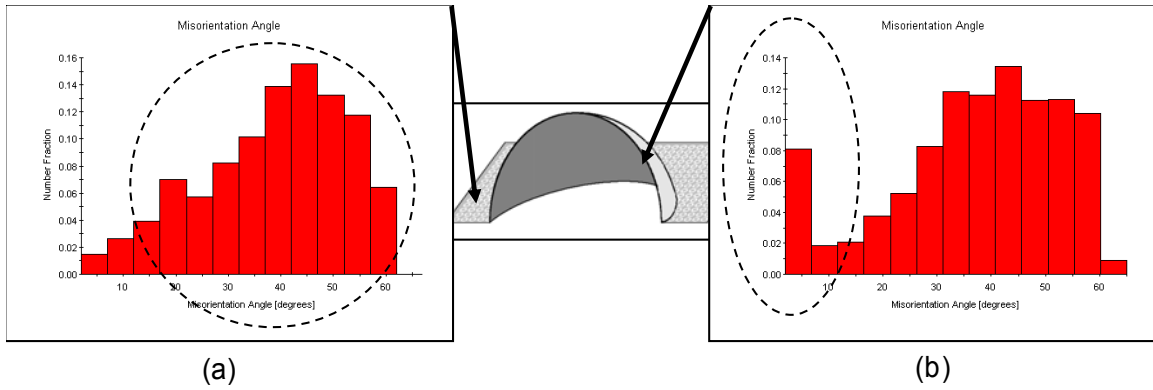around Position 9. The corresponding histograms for these data are shown in Appendix B.



(a)                                                                    (b)

Figure 22       Histograms for $10^{-2}$ s$^{-1}$ sample depicting (a) high-angle boundaries and (b) the occurrence of low-angle boundaries.
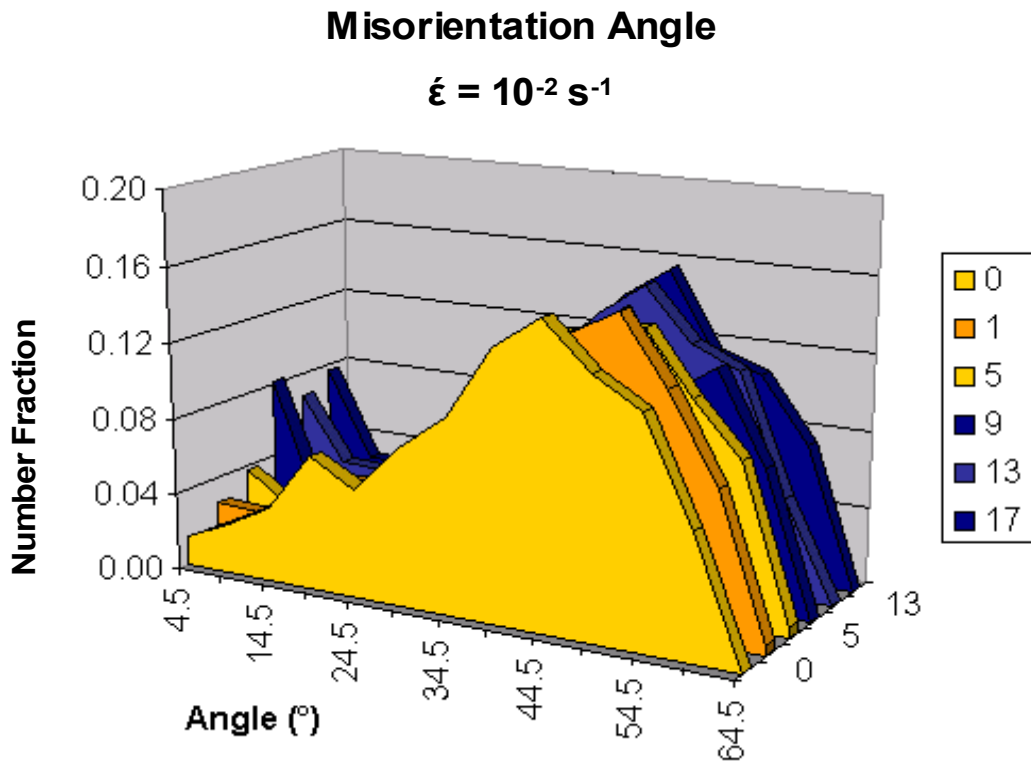


Figure 23       Misorientation angle distributions for 10-2 s-1

In this figure, the data denoted '0' are for the undeformed region, and the increasing numbers correspond to the positions described in the experimental

28

section; the location denoted '17' is near the pole of the dome.  The light colored plots depict a dominance of high-angle boundaries while the dark plots represent the data from the mid-latitudes onward and the development of low-angle boundaries.

The overall occurrence of low-angle boundaries under biaxial deformation was significantly less than that found under uniaxial deformation in the dislocation creep regime.  A possible reason for this is that the contribution of hydrostatic stress is greater under biaxial strain conditions than under uniaxial. Oh-ishi *et al.* (2004) found that

> A comparison of the disorientation distributions for biaxial deformation and uniaxial deformation, both in the dislocation creep regime, shows that the relative population of low-angle boundaries is *smaller* for dislocation deformation under *biaxial* conditions.  This suggests that cavity nucleation and growth may contribute a greater fraction of the strain during dislocation creep under biaxial conditions than under uniaxial conditions.  Under either loading condition, plastic deformation occurs when the maximum principal tension $\sigma_1 = \sigma_o$, where $\sigma_o$ is the flow stress.  However, the hydrostatic pressure under balanced biaxial tension is $\sigma_h = -\left(\frac{2}{3}\right)\sigma_o$, while it is $\sigma_h = -\left(\frac{1}{3}\right)\sigma_o$ under unixial tension.  For this reason processes leading to dilatiation will be expected to contribute more to the total strain under biaxial conditions than under uniaxial conditions [Ref. 27].

## C.    TEXTURE DEVELOPMENT

In an effort to confirm that texture development could be linked to dislocation creep, texture plots were generated for each location studied.  Below is a representation of a texture plot from the undeformed region of the lower $\dot{\varepsilon}$ sample and the corresponding <001> polar plot.  Due to symmetry in the texture, the chart shows texture intensity around the RD axis as a function of angles from 0 to 90°.  Here, high intensity at 0° corresponds to <001> directions aligned with the rolling direction, while intensity at 90° represents alignment in the plane of the sheet.  There is a weak residual texture from rolling which is indicated by the small peak at low-angles.
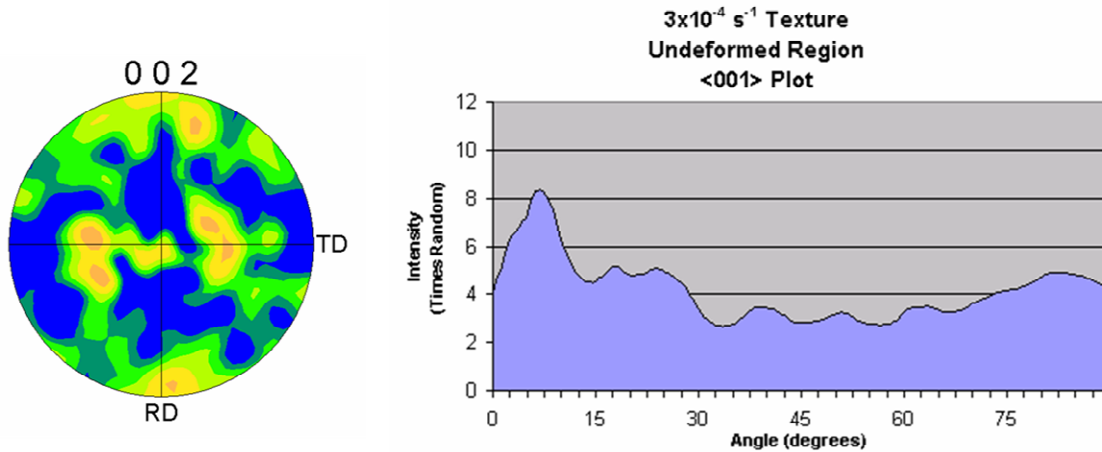
Figure 24    <001> Texture and Polar plot for undeformed region of lower strain rate sample.

For comparison purposes, <001> polar plots are shown collectively in Figure 25. Beginning with the undeformed region and working up toward the pole region, the plots are depicted in alternating light and dark colors, where the undeformed region is light and the pole position is dark. As stated previously, a weak orientation aligned with the rolling direction is left over from rolling and is shown in the '0' line. There is an initial relaxation of the rolling texture corresponding to grain boundary sliding. The weak texture then persists up the dome until approximately 75° (position 13). A significant rise in peak intensity at this position and the pole position depicts the onset of dislocation creep as the dominant deformation mechanism. The corresponding texture plots for this data are located in Appendix C.
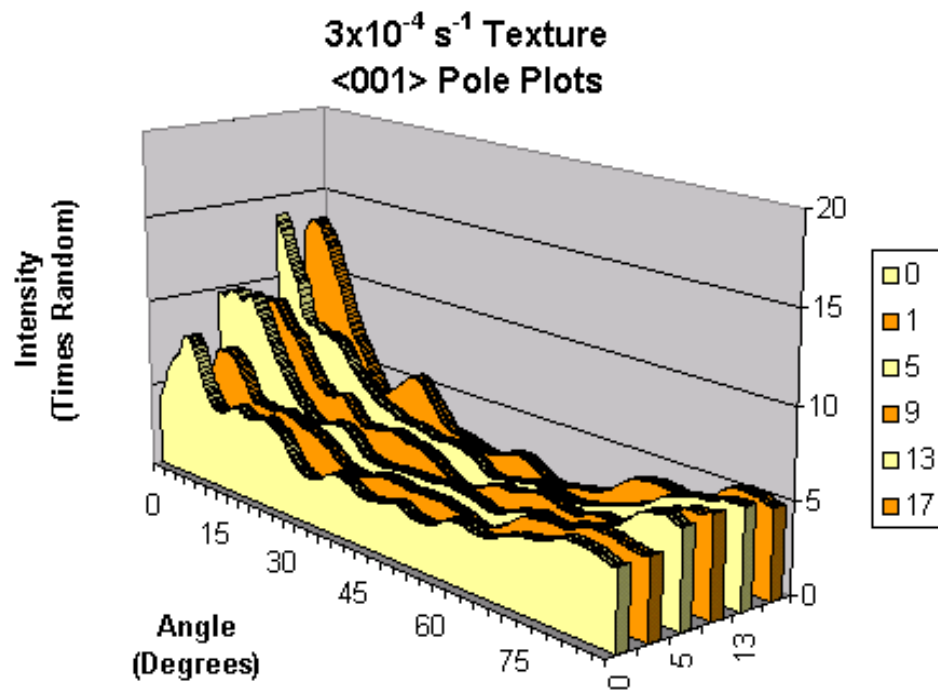
Figure 25     <001> Polar plots for 3x10$^{-4}$ s$^{-1}$ sample


Texture analyses for the lower nominal strain rate sample showed only the <001> fiber present which is reflected by the broad peak in the <111> distribution around 54° as shown in Figure 26.
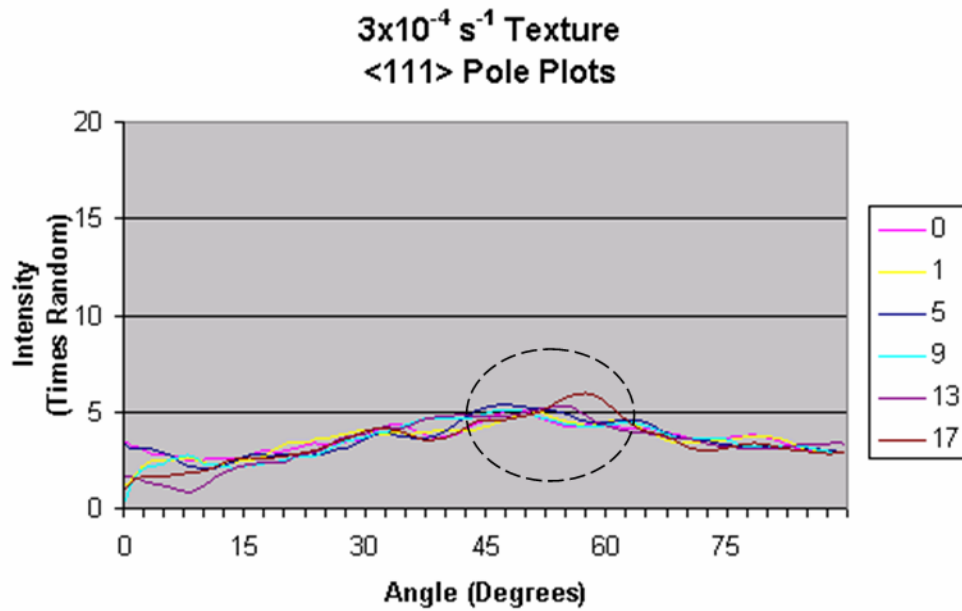
Figure 26     <111> Polar plots for 3x10$^{-4}$ s$^{-1}$ sample

Figure 27 is a representative pole figure from the undeformed region of the higher $\dot{\varepsilon}$ sample, and the corresponding <001> polar plot. Again, due to symmetry in the texture, the chart shows texture intensity around the RD axis as a function of angles from 0 to 90°. As in the previous low strain rate plots, a weak residual texture from rolling is apparent as indicated by the small peak at low-angles.
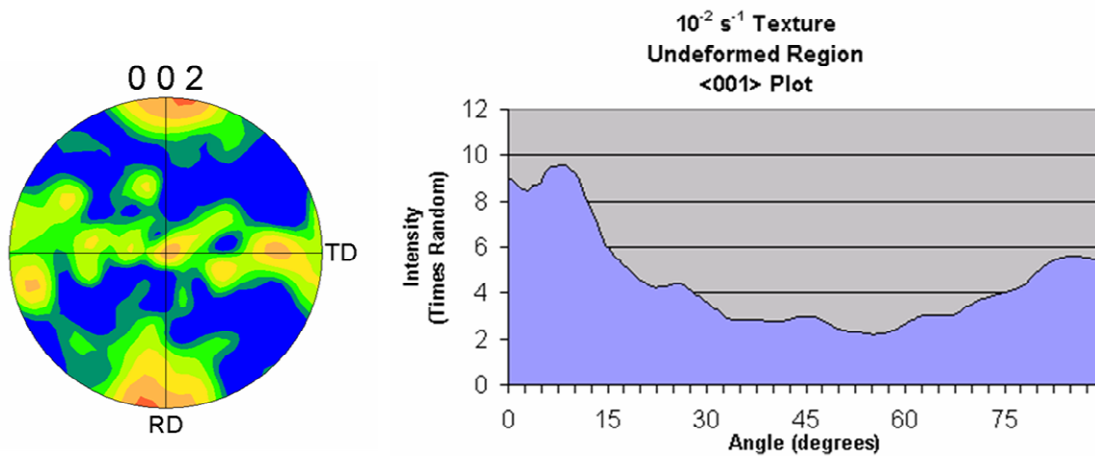


Figure 27     <001> Texture and Polar plot for undeformed region of higher strain rate sample.

The consolidated chart of <001> textures (Figure 28) for the higher strain rate sample shows essentially the same phenomenon as in the lower strain rate sample. The initial weak orientation persists up the dome until around 50˚ (position 9) at which point an increase in peak intensity indicates the onset of dislocation creep. The intensity of the preferred orientation is slightly greater throughout the measurements of the higher $\dot{\varepsilon}$ sample when compared to the lower $\dot{\varepsilon}$ sample. The corresponding texture plots for this data are located in Appendix D.
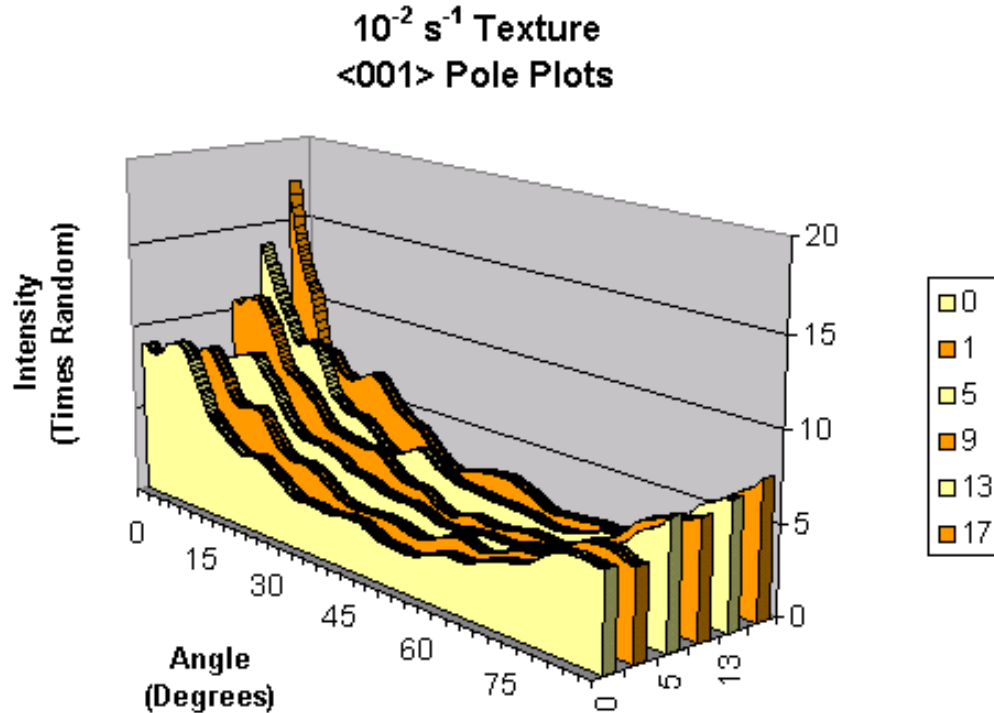


Figure 28      <001> Polar plots for $10^{-2}$ s$^{-1}$ sample

Texture analyses for the higher nominal strain rate sample showed the occurrence of a weak <011> fiber present in positions 9 through 17, from about 50˚ up to the pole. This fiber is apparent in the <011> polar plots (Figure 29) at 0˚

and 45˚.  It is also reflected by the peak in the <111> distribution around 35˚ as shown in Figure 30.
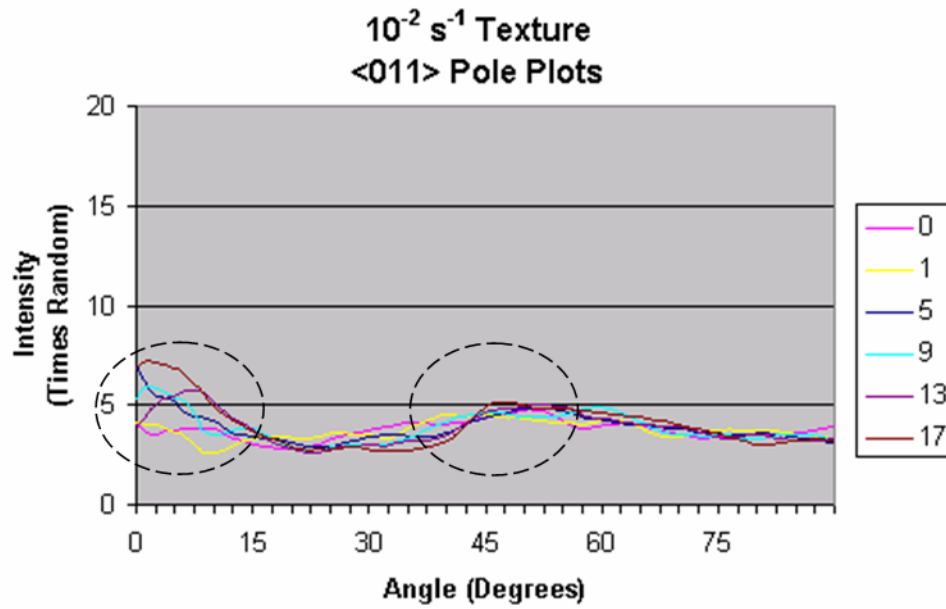


Figure 29     <011> Polar plots for $10^{-2}$ $s^{-1}$ sample



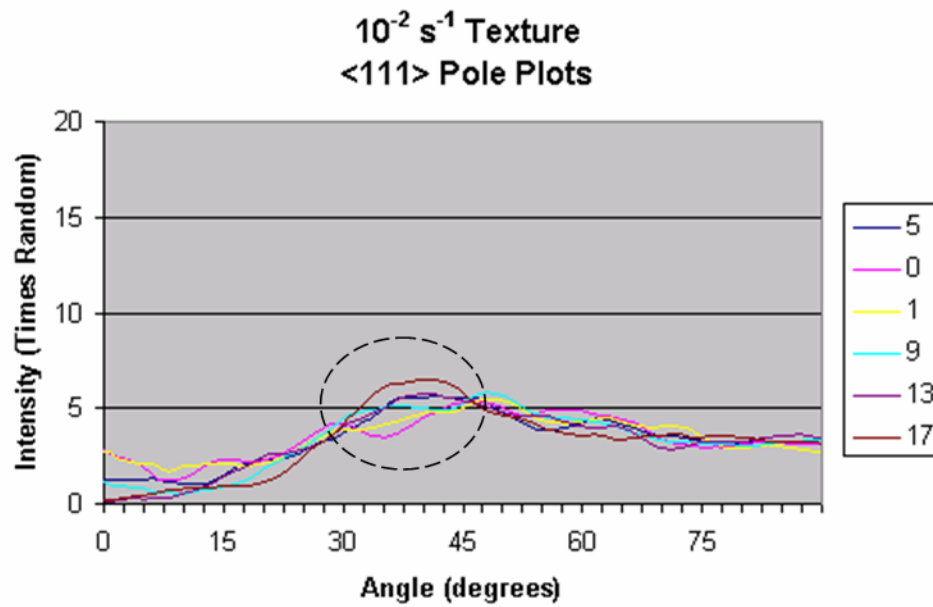Figure 30     <111> Polar plots for $10^{-2}$ $s^{-1}$ sample

# V.   DISCUSSION

The results achieved during this study are consistent with a transition in deformation mechanisms during superplastic dome forming.   These dome samples provide material that has experienced isochronal deformation.   Thus, different locations from the equator to the pole of the dome experience different strains and strain rates over the same time interval.   In the undeformed region as well as the clamped region, the material experiences only annealing effects. Near the equator and up to the mid-latitudes, the dome undergoes strains and strain rates below the nominal value for the dome deformation.

This occurred in the sample deformed at the lower nominal strain rate, $3x10^{-4}$ $s^{-1}$, in positions 1 – 5, which places them firmly in the GBS regime.   There is no evidence of subgrain boundary formation in the misorientation data for these points, and texture analyses show that the initial weak cube orientation is retained relatively unchanged as is consistent with deformation by GBS.   Data collected at the pole of this dome (position 17) show the formation of subgrains as well as a large peak in low-angle misorientations which signifies the transition to deformation by dislocation creep.   Also, at this location a distinct <100> fiber texture (parallel to the rolling direction) is evident which further indicates the transition to deformation by dislocation creep.   This suggests that the pole of the lower nominal strain rate sample was elevated into the transition region or even further into the dislocation creep regime (Figure 13).   A complicating factor at this location is the formation of large cavities;  the loss of load bearing cross-sectional area would result in local elevation of both strains and strain rates.   This would shift the local strain rates to even higher quantities within the dislocation creep regime.

The data for the higher nominal strain rate sample also suggest this variation in local rates around the nominal value.   The strain rate of $10^{-2}$ $s^{-1}$ should place the sample within the dislocation creep regime.   However, there was again a cube orientation in the clamped region due to recrystallization which

persisted in regions just above the dome.  This suggests that the local strain rates, which are below the nominal strain rate, were low enough to fall into the GBS regime or transition region (Figure 13).  In contrast, misorientation and texture data nearer the pole allude to the dominance of dislocation creep.  The occurrence of subgrains as well as the strengthening of the <100> fiber supports this supposition.  However, the texture only becomes slightly more distinct than that in material deformed under conditions nominally dominated by GBS.  This suggests that GBS may contribute well into the dislocation regime and may reflect the larger role that the hydrostatic stress plays in biaxial straining conditions versus uniaxial straining conditions.

Finally, since this research was done in an effort to achieve a representative overview of two domes formed under biaxial straining conditions, the microtexture data was obtained from approximately 25,000 data points for each position.  A better definition of texture development will likely require larger scan areas in selective regions to improve the statistics in defining the textures.

# VI.  CONCLUSIONS

1.  In the lower strain rate sample, a transition from grain boundary sliding to dislocation creep occurred at the pole of the dome as indicated by both misorientation angle data and fiber texture development.  The formation of low-angle boundaries in the material around cavities results in a higher number fraction between 0° and 15°.  This is due to local increases in strain and strain rate in ligaments between cavities.  The IQ maps indicate much larger cavities in lower strain rate sample than the higher strain rate sample.

2.  In the higher strain rate sample, the transition from grain boundary sliding to dislocation creep occurred at approximately 45° up the dome as indicated by both misorientation angle calculations and texture development.

3.  The overall occurrence of low-angle boundaries and texture development under biaxial deformation was significantly less than that found under uniaxial deformation in the dislocation creep regime.  This likely reflects the hydrostatic stress component which is greater during biaxial deformation than uniaxial deformation.

4.  The transition region in the $10^{-2}$ $s^{-1}$ sample occurred only slightly earlier than that in the $3\times10^{-4}$ $s^{-1}$ sample.  The expected increase in texture development from lower strain rate sample to higher strain rate sample was not as drastic under biaxial deformation conditions as uniaxial deformation conditions.

5.  Elongated grains that form during unixial tension did not form under biaxial straining conditions.  Grain growth was observed with subgrains parallel to both the thickness and the transverse directions.

6.  More grain growth was apparent in higher strain rate sample which spent less time at temperature.

7.      Texture formation in samples occurred in association with orientations in the initial weak texture which arose from thermomechanical treatments prior to deformation.

# VII. RECOMMENDATIONS

Further research in this area should

1. Include larger scan sizes of the regions in order to get a more complete picture of texture development. The average area scanned in this study was 25000 $\mu m^2$, while the average area scanned in selected cases previously [Ref. 5] was approximately 75600 $\mu m^2$.

2. Include more scans in the transition region to study more indepth the mechanisms at work.

3. Since the strain rates given for each sample were nominal values around the mid-latitudes, further research should look into the effects of local strain and strain rate history across the dome.

THIS PAGE INTENTIONALLY LEFT BLANK
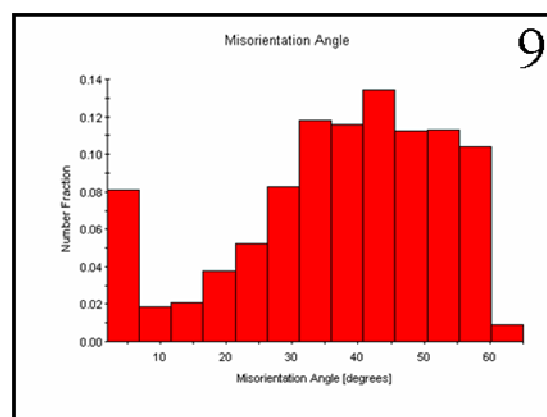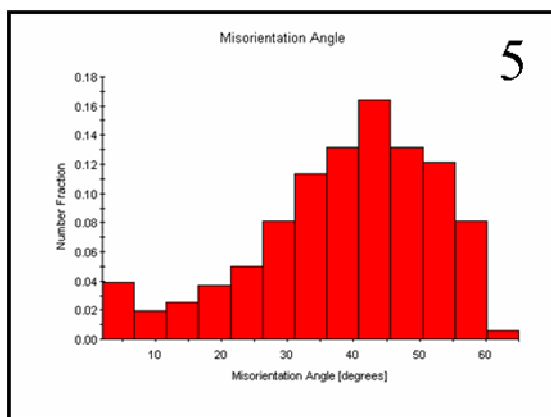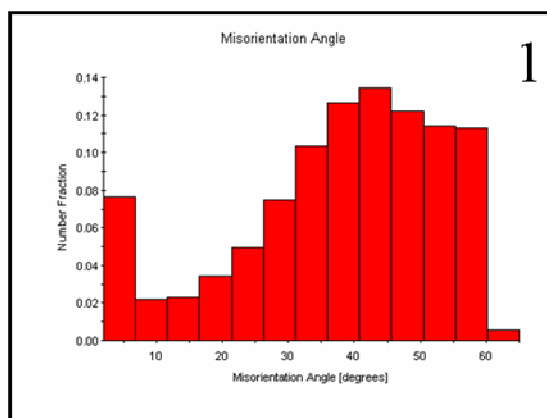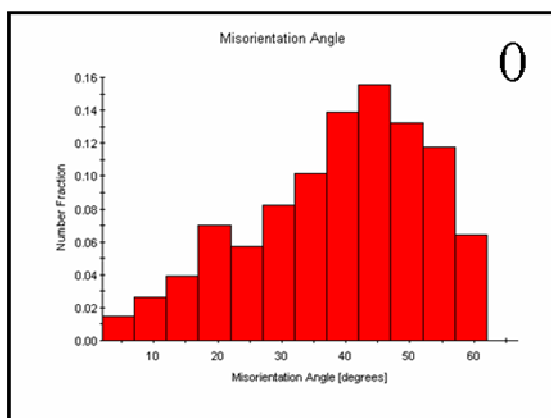
# LIST OF REFERENCES

1.  Ding, X.D., Zbib, H.M., Hamilton, C.H., Bayoumi, A.E., *J. Eng. Mat. Technol.*, v. 119, p. 26, 1997.

2.  Iwaski, H., Hosokawa, H., Mori, T., Tagata, T., Higashi, K., *Mat. Sci. Eng.*, v. A252, p. 199, 1998.

3.  Harrell, J.W., Analysis of the Transition in Deformation Mechanisms in Superplastic 5083 Aluminum Alloys by Orientation Imaging Microscopy, Master's Thesis, Naval Postgraduate School, Monterey, CA, September 2001.

4.  Secat, *Advanced Forming Techniques "Stretch" the Potential for Aluminum Sheet Applications* (2002 [cited 11 May 2004]); Available from the World Wide Web @ http://www.secat.net/tech%20adv%20tech%20stretch%20121302.php

5.  Boyden, J.F., Study of Cavitation and Failure Mechanisms of a Superplastic 5083 Aluminum Alloy, Master's Thesis, Naval Postgraduate School, Monterey, CA, September 2003.

6.  Chan, K.C., Tong, G.Q., *Scripta Mat.,* v. 38, p. 1705, 1998.

7.  Nieh, T.G., Wadsworth, J., and Sherby, O.D*., Superplasticity in Metals and Ceramics*, Cambridge University Press, New York, 1997.

8.  Verma, R., Friedman, P.A., Ghosh, A.K., Kim, S., Kim, C., *Metall. Trans. A*, v. 27A, p. 1889, 1996.

9.  Guo, K., Ridley, N., *Mat. Sci. Eng.*, v. A114, p. 97, 1989.

10. Pérez-Prado, M.T., González-Doncel, G., Ruano, O.A., and McNelley, T.R., *Acta Materialia*, v. 49, p. 2259, 2001.

11. Eddahbi, M., McNelley, T.R., Ruano, O.A., *Metall. Trans. A*, v. 32A, p. 1093, 2001.

12. *Secondary Electrons and Detection*, [cited 23 May 2004]; Available from the World Wide Web @ http://www.mse.iastate.edu/microscopy/secondary.html

13. Museum of Science, *Scanning Electron Microscope* [cited 23 May 2004]; Available from the World Wide Wed @ http://www.mos.org/sln/SEM/

14. Deffenbaugh, K., Private Communication

15. Edax TSL, *Electron Backscatter Diffraction and Orientation Imaging Microscopy* [cited 18 April 2004]; Available from the World Wide Web @ http://www.edax.com/TSL/index.html

16. TexSEM Laboratories, Inc. *OIM Analysis for Windows : User Manual*. 2000.

17. Randle, V., *Microtexture Determination and Its Applications*, The Institute of Materials, 1992.

18. Randle, V., Engler, O. *Texture Analysis: Macrotexture, Microtexture & Orientation Mapping*, Gordon and Breach Science Publishers, 2000.

19. Doherty, R.D., Hughes, D.A., Humphreys, F.J., Jonas, J.J., Juul Jenson, D., Kassner, M.E., King, W.E., McNelley, T.R., McQueen, H.J., Rollett, A.D., *Mat. Sci. Eng.,* v. A238, p. 219, 1997.

20. Taleff, E.M., McNelley, T.R., Unpublished report to the University of Texas, Austin, "Quarterly Report 9: AA 5083 Study", 2002.

21. McNelley, T.R., D.L. Swisher, Pérez-Prado, M.T., *Metall. Trans. A*, v. 33A, p. 279, 2002.

22. Chan, K.C., Chow, K.K., *Int. J. Mech. Sci.,* v. 44, p. 1467, 2002.

23. Hsiao, I.C., Huang, J.C., *Scripta Materialia*, v. 40 (6), p. 697, 1999.

24. Taleff, E.M., McNelley, T.R., Unpublished report to the University of Texas, Austin, "Quarterly Report 5: AA 5083 Study", 2001.

25. Kulas, M., Krajewski, P.E., McNelley, T.R., Taleff, E.M, Unpublished report to the University of Texas, Austin, "Deformation and Failure Mechanisms in Commercial AA5083 Materials".

26. Bradley, J.R., "Bulge Testing of Superplastic AA5083 Aluminum Sheet", *Advances in Superplasticity and Superplastic Forming,* 2004.

27. Oh-ishi, K., Boyden, J.F., McNelley, T.R., "Deformation Mechanisms and Cavity Formation in Superplastic AA5083", *Advances in Superplasticity and Superplastic Forming,* 2004.

28. Taleff, E.M., McNelley, T.R., Unpublished report to the University of Texas, Austin, "Quarterly Report 10: AA 5083 Study", 2003.

29. Taleff, E.M., McNelley, T.R., Unpublished report to the University of Texas, Austin, "Quarterly Report 11: AA 5083 Study", 2003.

30. Taleff, E.M., McNelley, T.R., Unpublished report to the University of Texas, Austin, "Quarterly Report 12: AA 5083 Study", 2003.

31. Taleff, E.M., McNelley, T.R., Unpublished report to the University of Texas, Austin, "Quarterly Report 13: AA 5083 Study", 2003.

32. Marciniak, Z., Kucznski, K., *Int. J. Mech. Sci.,* v. 9, p. 609, 1967.

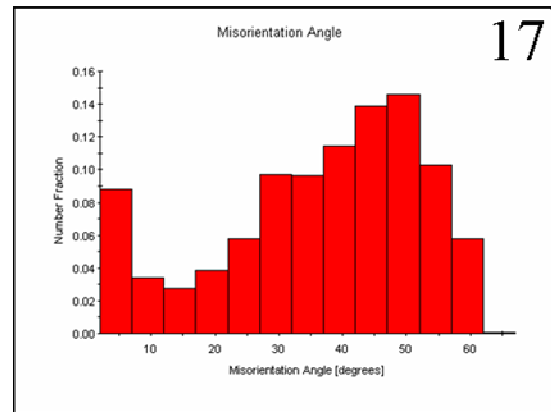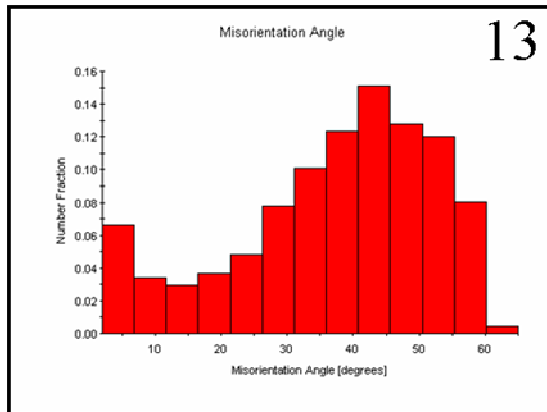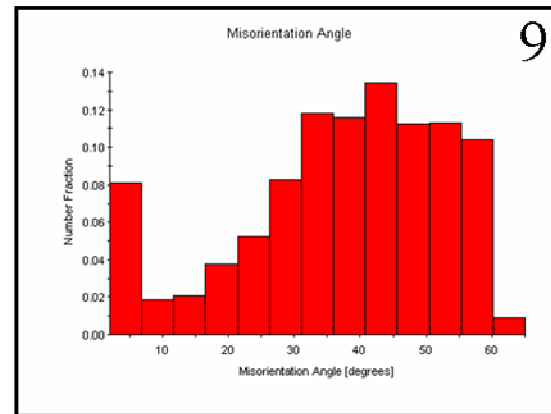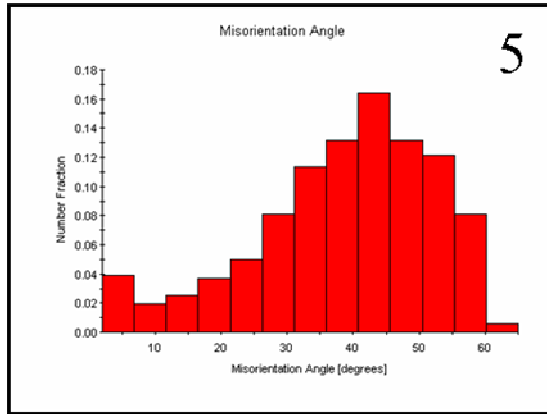33. Rees, D.W., *Int. J. Mech. Sci.,* v. 37, p. 373, 1995.

THIS PAGE INTENTIONALLY LEFT BLANK

# APPENDIX A     MISORIENTATIONS 3X10<sup>-4</sup> S<sup>-1</sup>
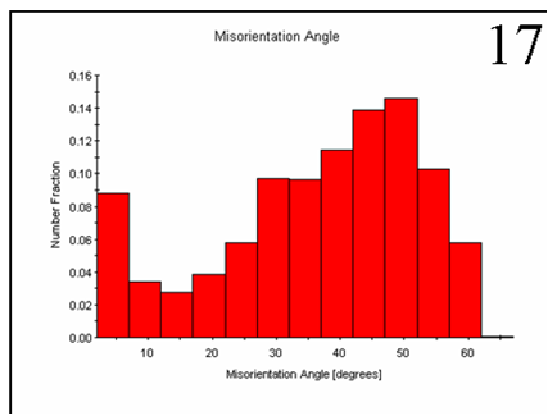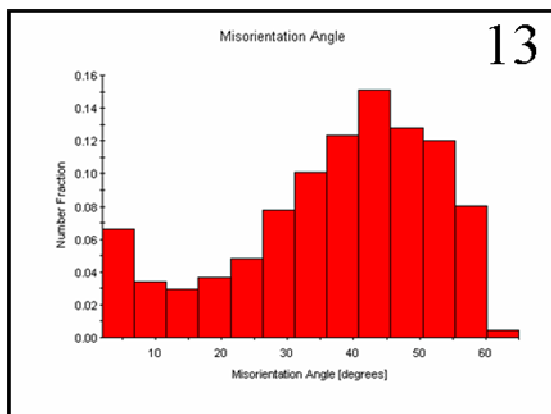
THIS PAGE INTENTIONALLY LEFT BLANK

Misorientation Angle — 0



Misorientation Angle — 1



Misorientation Angle — 5



Misorientation Angle — 9



Misorientation Angle — 13



Misorientation Angle — 17
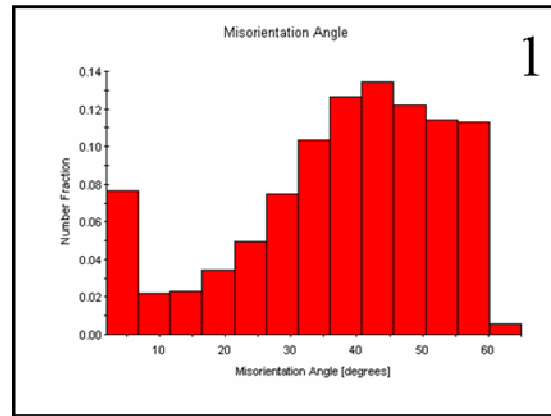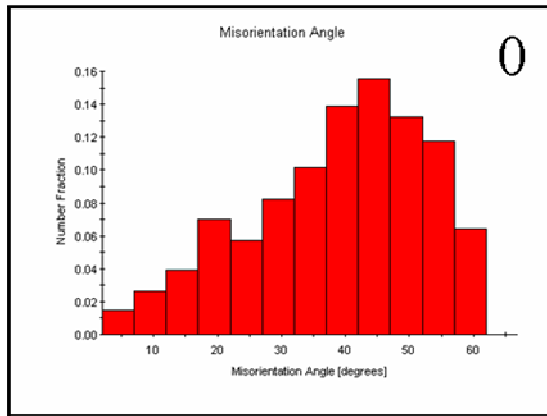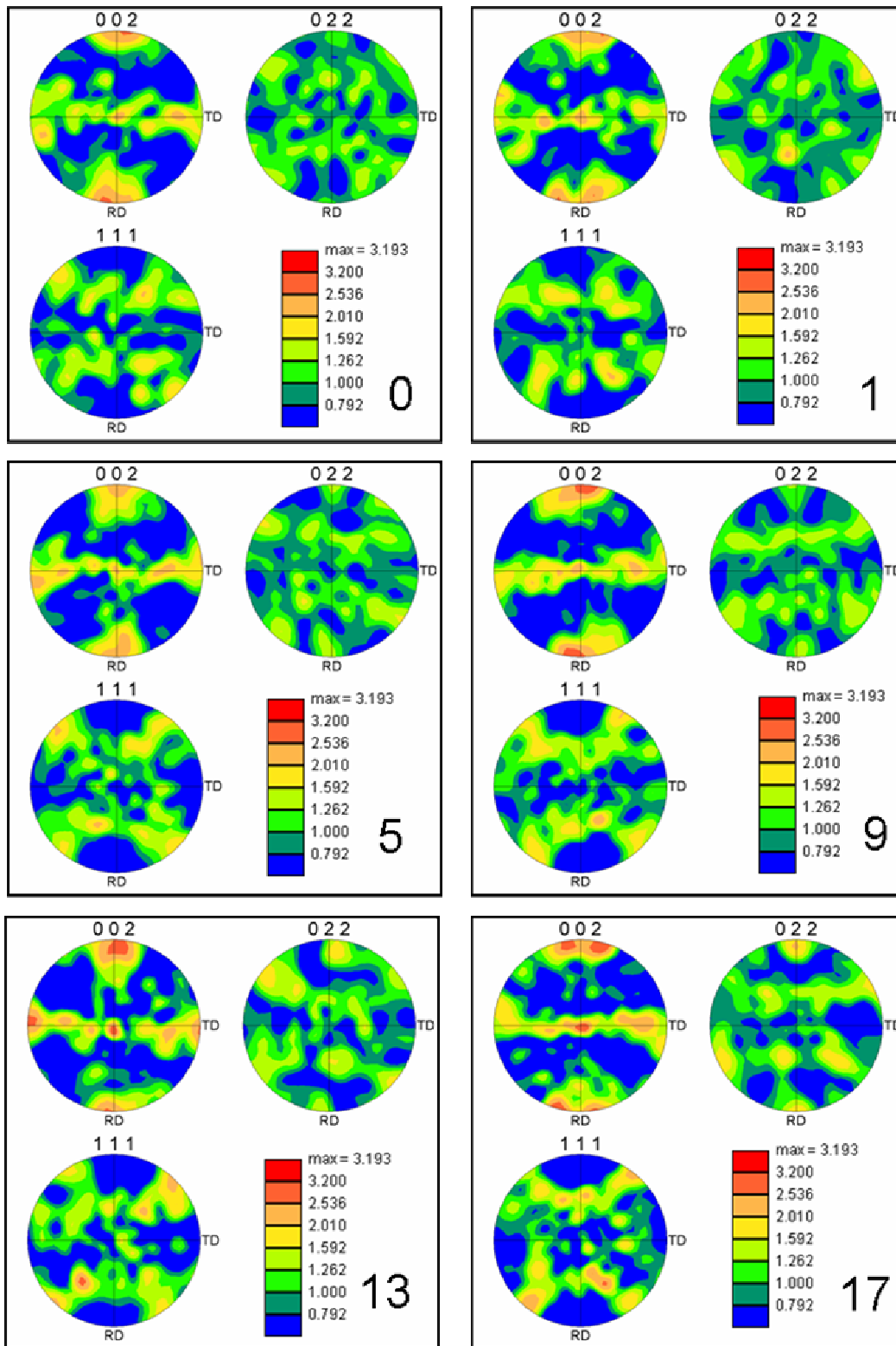
THIS PAGE INTENTIONALLY LEFT BLANK

# APPENDIX C     3X10<sup>-4</sup> S<sup>-1</sup> <001> TEXTURE PLOTS
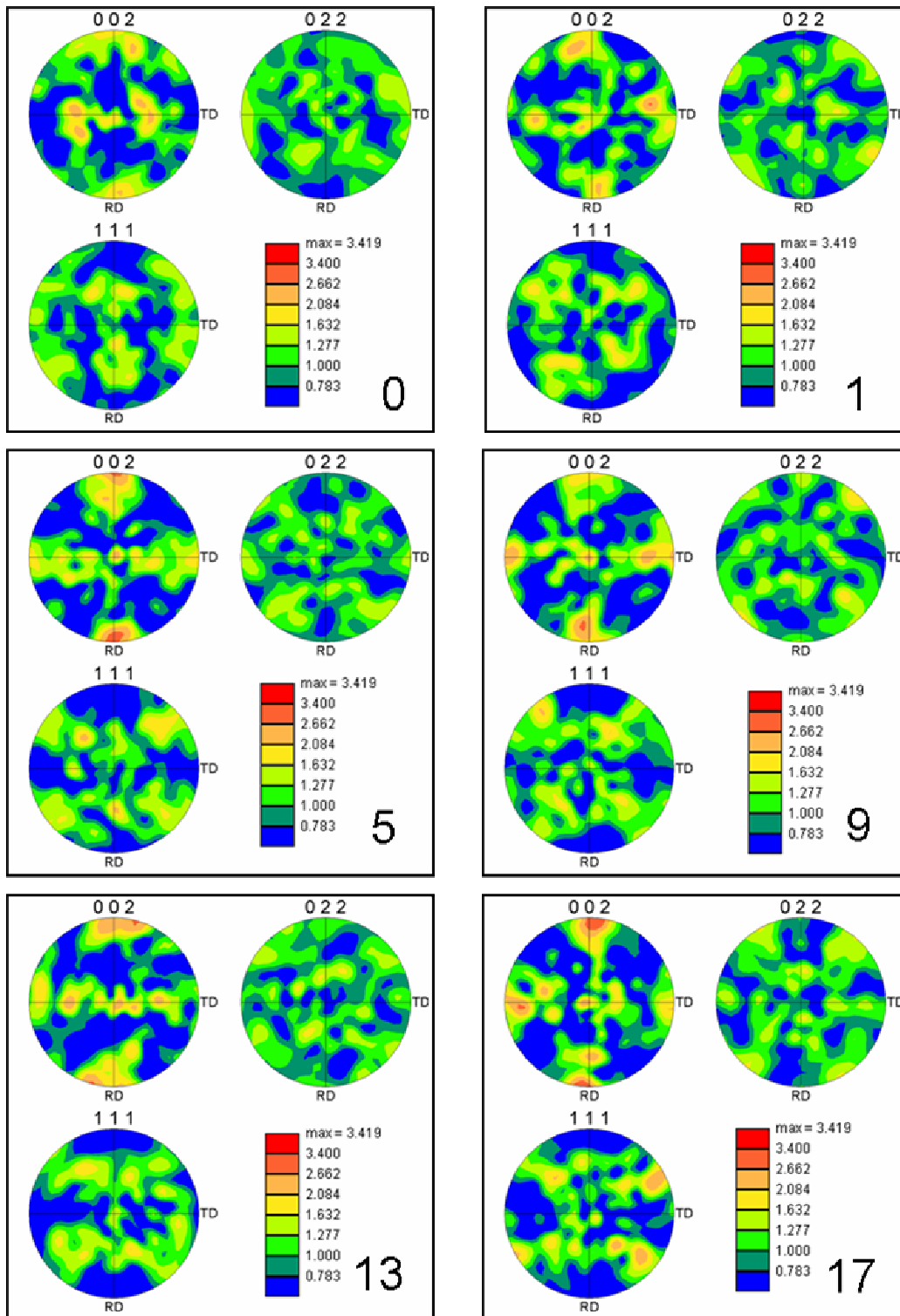
THIS PAGE INTENTIONALLY LEFT BLANK

# APPENDIX D     10$^{-2}$ S$^{-1}$ <001> TEXTURE PLOTS

THIS PAGE INTENTIONALLY LEFT BLANK

# INITIAL DISTRIBUTION LIST

1. Defense Technical Information Center
   Ft. Belvoir, Virginia

2. Dudley Knox Library
   Naval Postgraduate School
   Monterey, California

3. Engineering and Technology Curricular Office, Code 34
   Naval Postgraduate School
   Monterey, California

4. Department Chairman, Code ME/Hy
   Naval Postgraduate School
   Monterey, California

5. Professor Terry R. McNelley, Code ME/Mc
   Naval Postgraduate School
   Monterey, California

6. Dr. Keiichiro Oishi, Code ME/Oi
   Naval Postgraduate School
   Monterey, California

7. Dr. Alex Zhilyaev, Code ME
   Naval Postgraduate School
   Monterey, California

8. Professor Eric Taleff
   The University of Texas at Austin
   Austin, Texas

9. Dr. Paul E. Krajewski
   General Motors Corporation
   Warren, Michigan

10. ENS Rebecca M. Fowler
    Naval Postgraduate School
    Monterey, California